Reviewer1:

Interactive comment on "Emission, transport and radiative effects of mineral dust from Taklimakan and Gobi Deserts: comparison of measurements and model results" by Siyu Chen et al.

This manuscript presented the WRF-CHEM modeling results of Emission, transport and radiative effects of mineral dust from Taklimakan and Gobi Deserts based on the validation with the measurements of CALIPSO Aerosol Extinction Coefficients and AERONET-AOD as well as the available meteorological observation. It is especially interesting to compare the differences in regional dust transport from two major deserts in Taklimakan and Gobi regions for understanding on Asian dust aerosols and their climate effect. Therefore this manuscript could fall within the scope of ACP. I suggest the minor revisions before it is published as follows:

We thank the reviewer for the constructive suggestions. Both text and figures have been revised as suggested.

1) Please give more discussions on the effect of basin terrain on dust emissions and transport over the Taklimakan Deserts, where the simulated dust emissions are over-estimated due to the larger near-surface winds (Lines: 265-267: The simulated wind speed (6.4 m s^{-1}) was higher than the observed wind speed (4.7 m s^{-1})). How are the influences of the overestimated dust emissions and the unique boundary layer in the basin atmosphere on TD dust transport?

Thank you so much for your suggestions. The TD is the location of the second largest shifting sand desert in the world and covers an area of 337,000 km^2, approximately 85% of which is covered by shifting sand dunes [Ge et al., 2014]. It is located in the Tarim Basin and is surrounded by the Kunlun Shan Mountains (average elevation 5.5 km) to the south, the Tianshan Mountains (average elevation 4.8 km) to the north and the Pamir Plateau (average elevation 5.5 km) to the west. Therefore, dust particles in the TD were transported from the east of Tarim basin due to the barrier of surrounding mountains. The transport contribution of the TD dust (1.1 ton day^{-1}) to the dust sink was smaller than that of the GD dust (1.4 ton day^{-1}). It is noted that the TD is not the main source region in China but a small amount of the TD dust was lofted to more than 5 km and transported over greater distances under the influence of the westerly jets.

At the Yumenzhen site，the prevailing wind direction was generally from the east. The simulated wind speed (6.4 m s^{-1}) was higher than the observed wind speed (4.7 m s^{-1}) in the simulations. We think that the different frequencies of wind speed and direction between the observations and WRF-Chem model might have partly contributed to the deviations in the results. Moreover, no denying that an overestimation in simulated surface winds in WRF model is a common issued due to model limitations in representation turbulence processes and sub-grid variation in terrain and land surface type (Hanna et al., 2000). Although simulations overestimate the magnitude of observed 10-m wind speed over the TD and GD, it could reproduce the observed spatial distribution of 10-m wind speed over dust source regions over East Asia. Therefore, we could tune the value of the empirical proportionality constant C in the GOCART dust emission schemes to keep the magnitude of modeled AOD consistent with the observational data. The value of C was set to 1 μg s^{2} m^{-5} in the study. We can found that WRF-Chem model well capture the spatial distribution of AOD over East Asia, especially in dust source regions. Fig. 4 showed that MODIS retrievals could be compared to the simulated AOD over East Asia, although the datasets were not insufficient because of their limited spatial and temporal coverage. The average MODIS AOD and simulated AODs over the TD and GD were 0.88 and 0.82, respectively. The modelling results generally captured the observed AODs from the MODIS retrievals over the dust source region, indicating that the GOCART dust emissions represented dust emission and dust transport under the boundary layer over the TD well. Now we have clarified in the corresponding description by adding the following statement "*Although simulations overestimate the magnitude of observed 10-m wind speed over the TD and GD, it could reproduce the observed spatial distribution of 10-m wind speed over dust source regions over East Asia. Therefore, we could tune the value of the empirical proportionality constant C in the GOCART dust emission schemes to keep the magnitude of modeled AOD consistent with the observational data. The value of C was set to 1 μg s^{2} m^{-5} in the study.*"

2) Please improve the quality of figures and clarify the captions:

a) Fig.1: the color bars around 2000m and higher than 5800m are almost same

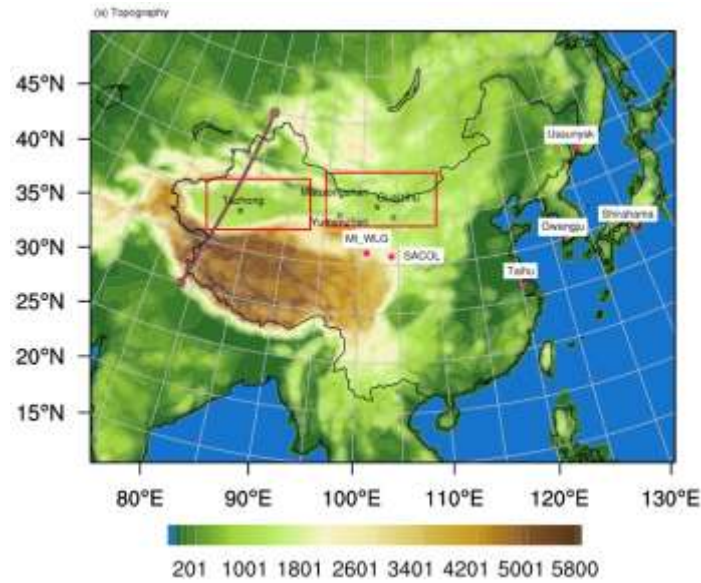Thank you so much for your suggestions. We have changed the color bars.

Fig. 1 (a) Modelling domain and spatial distribution of the topography over East Asia. Taklimakan Desert (TD) and Gobi Desert (GD) are indicated by the red boxes. The pink dots are the AERONET sites (SACOL, Mt. Waliguan (Mt_WLG), Taihu, Gwangju_GIST, Shirhuma and Ussuriysk). The black stars are the sites with observed 10-m winds (Tazhong, Maozongshan, Yumenzhen, and Guaizihu). The blown line represents the orbit path of CALIPSO/CALIOP over the TD at 0:08 UTC (2:08 LT) on 19th March 2010. (b) Soil erodibility used in GOCART dust emission scheme from WRF-Chem model.

b) Fig 3: the number size is too small to be seen.

Thank you so much for your suggestions. We have revised it. The revised figure is as follow:
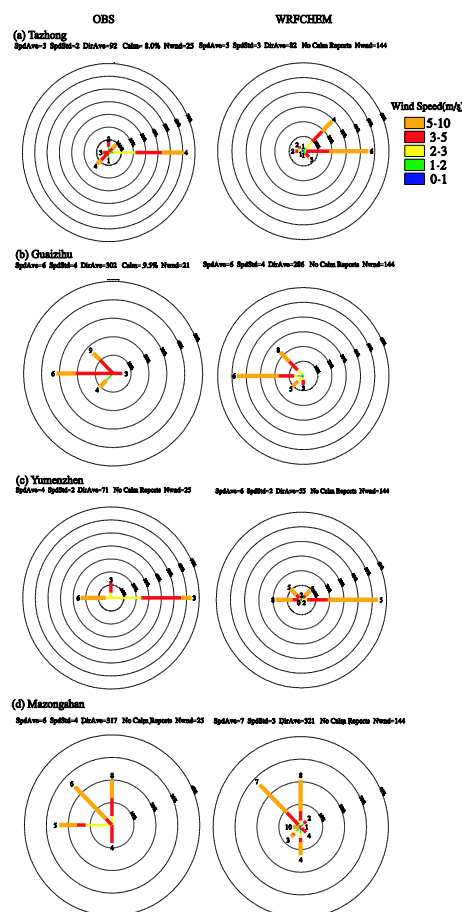
Fig. 3 Wind rose diagrams at the four meteorological stations: Tazhong (a), Guaizihu (b), Yumenzhen (c), and Maoyinbadao (d) over the TD and GD during the simulation period from observations and WRF-Chem model. The mean wind speed is included at the end of each directional line.

c) Fig 5: are any similar plots over the Gobi Deserts?

Thank you so much for your suggestion. Unfortunately, we can not find cross-sections of aerosol extinction coefficients at 532 nm over the Gobi Deserts from CALIPSO retrievals in the simulation periods.

c) Fig 11: the meanings of solid and dash lines?

Thank you so much for your suggestions. The solid lines represent temperature and dash lines represent dew point temperature. It is clarified in currently Fig. 12 "*Fig.12 The skew T-log diagram over the TD (black lines) and GD (Red lines) on 19th March 2010 from the WRF-Chem simulation. The solid lines represent temperature and dash lines represent dew point temperature.*"

d) Fig 12: Please clarify the estimations of dust mass balance and transport. Should be the negative and positive values equal?

Thank you so much for your suggestions. To better understand the relative contribution of dust emissions over the TD and GD during the dust storm event, currently Fig. 13 shows that the budgets for dust emission, transport, and dry and wet depositions over the TD and GD, respectively. The positive sign represents increase to dust concentration and the negative sign represents decrease to dust concentration. Among the four budget terms, the source term of the dust concentration was the absolute dust emission for the entire dust storm event over the TD and GD. Therefore, emission contribution is absolute positive. While dry/wet depositions as well as transport are sinks of dust in the atmosphere, these values are always negative. Dry deposition is the largest sink of dust, following by transport and wet deposition. Now we have clarified in the corresponding description by adding the following statement "*To better understand the relative contribution of dust emissions over the TD and GD during the dust storm event, Fig. 13 shows that the budgets for dust emission, transport, and dry and wet depositions over the TD and GD, respectively. The positive sign represents increase to dust concentration and the negative sign represents decrease to dust concentration. Among the four budget terms, the source term of the dust concentration was the absolute dust emission for the entire dust storm event over the TD and GD. Therefore, emission contribution is absolute positive. While dry/wet depositions as well as transport are sinks of dust in the atmosphere, these values are always negative. Dry deposition is the largest sink of dust, following by transport and wet deposition.*" "*Specifically, the GD dust emission was the largest contributor to dust concentration over East Asia in the first stage (18th-20th March) (Fig. 13). The daily dust emission flux over the GD peaked above 68 μg m^{-2} s^{-1} (Fig. 9). The contribution of the transport of the GD dust particles (up to 3.4 ton day^{-1}) was much greater than that of the TD dust (up to 1.5 ton day^{-1}) (Fig. 13). The strengthening dust emissions weakened substantially in the second stage (21st-23rd March). The TD dust emission exerted an important effect on dust concentrations in that stage. The average TD dust emission flux was 20±4.6 μg m^{-2} s^{-1} (Fig. 9). Dry deposition was the largest sink over the TD, and wet deposition was much smaller over the TD and GD (Fig. 13).*"

e) Fig. 13: what do the dash lines stand for?

Thank you so much for your suggestions. The dash lines stand for potential

3) Please check the English grammar (for example: line 328: plays a very important role)

Thank you so much for your suggestions. We have check again in the whole paper.

References:

- Ge J., J. Huang, C. Xu, Y. Qi, and H. Liu, 2014: Characteristics of Taklimakan dust emission and distribution: A satellite and reanalysis field perspective. Journal of Geophysical Research: Atmospheres, 119, 11,772–11,783, doi:10.1002/2014JD022280.
- Hanna, S.R., Yang, R., Yin, X., 2000. Evaluations of numerical weather prediction (NWP) models from the point of view of inputs required by atmospheric dispersion models. Int. J. Environ. Pollut. 14 (1–6), 98–105.

Emission, transport and radiative effects of mineral dust from Taklimakan and Gobi Deserts: comparison of measurements and model results

Siyu Chen[1], Jianping Huang[1*], Litai Kang[1], Hao Wang[1], Xiaojun Ma[1], Yongli He[1], Tiangang Yuan[1], Ben Yang[2], Zhongwei Huang[1], and Guolong Zhang[1]

[1] Key Laboratory for Semi-Arid Climate Change of the Ministry of Education, Lanzhou University, Lanzhou, China

[2] School of Atmospheric Sciences, Nanjing University, Nanjing, China

*Corresponding author: Jianping Huang; phone: 0931-8914139;

Email: hjp@lzu.edu.cn

Abstract

The weather research and forecasting model with chemistry (WRF-Chem) was used to investigate a typical dust storm event that occurred from 18th to 23rd March 2010 and swept across almost all of China, Japan, and Korea. The spatial and temporal variations in dust aerosols and the meteorological conditions over East Asia were well reproduced in WRF-Chem model. The simulation results were used to further investigate details of processes related to dust emission, long-range transport, and radiative effects of dust aerosols over the Taklimakan desert (TD) and Gobi desert (GD). The results showed that weather conditions, topography and surface types in dust source regions may influence dust emission, uplift height and transport at regional scale. The GD was located in the warm zone in advance of the cold front in this case. Rapidly warming surface temperatures and cold air advection at high levels caused strong instability in the atmosphere which strengthened the downward momentum transported from the middle and low troposphere and caused strong surface winds. Moreover, the GD is located in relatively flat, high altitude regions influenced by the confluence of the northern and southern westerly jets. Therefore, the GD dust particles were easily lofted to 4 km and were the primary contributor to the dust concentration over East Asia. In the dust budget analysis, the dust emission flux over the TD was 27.2±4.1 μg m^{-2} s^{-1}, which was similar to that over the GD (29±3.6 μg m^{-2} s^{-1}). However, the transport contribution of the TD dust (up to 0.8 ton day^{-1}) to the dust sink was much smaller than that of the GD dust (up to 3.7 ton day^{-1}) because of the complex terrain and the prevailing wind in the TD. It is noted that a small amount of the TD dust (PM$_{2.5}$ dust concentration was approximately 8.7 ug m^{-3}) was lofted to more than 5 km and transported over greater distances under the influence of the westerly jets. Moreover, the direct radiative

forcing induced by dust was estimated as -3 W m^{-2} and -7 W m^{-2} at the top of the atmosphere, -8 W m^{-2} and -10 W m^{-2} at the surface, and +5 W m^{-2} and +3 W m^{-2} in the atmosphere over the TD and GD, respectively. The study provided confidence for further understanding the climate effects of the GD dust.

Key words: East Asian dust, Dust modelling, WRF-Chem model, Taklimakan desert, and Gobi desert

1. Introduction

Dust is regarded as a major component of tropospheric aerosols in the global atmosphere [Forster et al., 2007; Zhang et al., 2003; Bi et al., 2011]. It is considered to have a significant direct effect on climate by altering the radiative balance between the incoming solar and outgoing planetary radiation in the atmosphere [Ramanathan et al., 2001; Huang et al., 2008a, b, c, 2009, 2010, 2011; Fu et al., 2009; Han et al., 2012; Zhao et al., 2013; Chen et al., 2014b]. In addition, dust can also indirectly modify the microphysical properties of clouds by influencing cloud condensation nuclei and ice cores and thus influence precipitation efficiency [Koren et al., 2004; Huang et al., 2006a, b, c, 2010, and 2014; Su et al., 2008; Qian et al., 2009; Li et al., 2010]. Therefore, dust aerosols have important roles in changing the energy budget and atmospheric and hydrological system at regional and even global scales [Wang et al., 2010; Wang et al., 2012; Huang et al., 2010, 2014; Li et al., 2011; Zhao et al., 2011, 2012].

East Asian dust is entrained from China and its surrounding regions, which constitute the second largest contributor to global dust aerosols [Rea, 1994; Zhang et al., 2003; Ye et al., 2012]. The Taklimakan desert (TD) and Gobi desert (GD) are regarded as two major dust source

249　regions in East Asia (Fig. 1a) [Sun et al., 2001]. The TD is the location of

250　the second largest shifting sand desert in the world and covers an area of

251　337,000 km^2, approximately 85% of which is covered by shifting sand

252　dunes [Ge et al., 2014]. It is located in the Tarim Basin and is surrounded

253　by the Kunlun Shan Mountains (average elevation 5.5 km) to the south,

254　the Tianshan Mountains (average elevation 4.8 km) to the north and the

255　Pamir Plateau (average elevation 5.5 km) to the west. The GD covers

256　parts of northern China, northwestern China, and southern Mongolia,

257　which is bounded by the TD in the west, the North China Plain in the

258　southeast, and the Hexi Corridor and Tibetan Plateau in the southwest.

259　　Airborne dust over the TD may play an important role in the global

260　radiative energy budget [Huang et al., 2009, 2015]. Special efforts have

261　been dedicated to understanding the spatial and temporal features of the

262　TD dust [Liu et al., 2016], including dust emission [Zhang et al., 2003;

263　Zhao et al., 2003, 2006a; Shao et al., 2011; Chen et al., 2013, 2014a;

264　Xiong et al., 2013], long-range transport [Uno et al., 2001; Han et al.,

265　2005, 2006, 2008; Zhao et al., 2006b, 2007; Huang et al., 2007], dust

266　radiative forcing [Takamura et al.,2004, 2005; Su et al., 2008; Huang et

267　al., 2009; Ye et al., 2012], and its climatic effects [Huang et al., 2006a, b,

268　2007, 2010 ,2014] over the TD. However, few of these studies have

269　investigated the role of GD dust in the earth-atmosphere system,

270　especially concerning the differences and similarities of dust emission

271　and transport over the GD and TD. Using dust storm reports of 1960-

272　1999, Sun et al. (2001) have found that the GD is the dominant dust

273　source region for East Asia. The dust deposited over East Asia including

274　the Loess Plateau in China and offshore regions. Using Cloud-Aerosol

275　Lidar and Infrared Pathfinder Satellite Observation (CALIPSO) and

276　surface measurements, Huang et al. (2008) have found that dust events

are more frequent over the TD, where suspended dust was dominant locally, whereas GD dust storms were less frequent but more intensive. Zhang et al. (2008) have showed that the GD accounted for more than 75% of the dust emission events in all of East Asia using time-series of Multi-angle Imaging SpectroRadiometer (MISR) images. However, it is difficult to use observational data to quantify the details of TD and GD dust emission fluxes and to distinguish the contributions of the TD and GD to dust transport in the downwind deposition regions of East Asia.

In this study we focused on a state-of-the-art model that simulates detailed dust processes to investigate a typical dust event over East Asia that occurred on 18th-23rd March 2010. This dust storm is the strongest since 2006, in terms of scope, intensity and duration of activities. It swept across almost 21 provinces in China, covering an area of 282×104 km^2 and affected about 2.7×10^8 people. Dust particles have even been long-range transported to Shenzhen, Hong Kong and Taiwan. Due to its strong influence, Hong Kong reported an air pollution index exceeded 400 and Shen Zhen also have a heavily polluted day in 19th March 2010 [Li et al., 2012].

The aim of this work was to (1) evaluate the ability of the weather research and forecasting model with chemistry (WRF-Chem) to reproduce East Asian dust relative to observational data; (2) investigate the dynamic and thermodynamic mechanisms of dust emission and transport over the TD and GD; (3) elucidate the influence of TD and GD dust throughout East Asia; and (4) estimate the direct radiation forcing induced by the TD and GD dust over East Asia. The paper is organized as follows. The model and observational data are described in Sections 2 and 3. The model evaluation and a discussion of the emission and transport of East Asian dust are presented in Section 4. The radiative

305　forcing of dust is estimated in Section 5 followed by the discussion and

306　conclusions in Section 6.

2. Model description

308　　WRF-Chem, which simultaneously simulates trace gases, particulate

309　materials and meteorological fields [Skamarock et al., 2008], was used in

310　this study. Gas-phase chemical mechanisms, photolysis schemes and

311　aerosols schemes are incorporated into the WRF-Chem model, which

312　considers a variety of coupled physical and chemical processes such as

313　emission, transport (advection, diffusion, and convection), dry/wet

314　deposition, chemical transport, aerosol interactions, and radiation budget

315　[Grell et al., 2005]. Compared with other numerical models, the "online"

316　coupling of meteorology and chemistry in the WRF model more

317　accurately represents the evolution of trace gases and aerosols and

318　permits the inclusion of detailed feedback processes for weather or

319　climate change. Details of the model and relevant references can be found

320　at　　　　http://www.pnl.gov/atmospheric/research/wrf-chem/　　　and

321　http://www.pnl.gov/atmospheric/research/wrf-chem/publications.stm，

322　respectively.

323　　The Regional Acid Deposition Model version 2 chemical

324　mechanism and Model Aerosol Dynamics Model for Europe and

325　Secondary Organic Aerosol Model (MADE/SORGAM) aerosol model

326　[Ackermann et al., 1998; Schell et al., 2001] were implemented by Grell

327　et al. [2005] into WRF-Chem, which includes some aqueous reactions

328　and　complex　treatments　of　aerosol　radiative　properties.

329　MADE/SORGAM model uses the modal approach with Aitken,

330　accumulation, and coarse modes to represent the aerosol size distribution.

331　The aerosol species include mineral dust, sulfate, nitrate, ammonium,

332　black carbon, organic compounds, and sea salt. Aerosol optical properties

(e.g., single-scattering albedo, asymmetry factor, and extinction) are computed as a function of wavelength. Furthermore, each chemical constituent of the aerosol is associated with a complex index of refraction [Barnard et al., 2003].

The Goddard Chemistry Aerosol Radiation and Transport (GOCART) dust emission scheme [Ginoux et al., 2001] was coupled with MADE/SORGAM in the WRF-Chem model [Zhao et al., 2010]. Additional details about the GOCART dust emission scheme in the WRF-Chem model can be found in Chen et al. [2013 and 2014]. An emission inventory of anthropogenic, biomass burning, biogenic, and volcanic emissions is also included in the simulation. The anthropogenic emissions of carbon monoxide, nitrogen oxides, SO_2, volatile organic compounds, black carbon, organic carbon, $PM_{2.5}$, and PM_{10} were taken from the 2006 emission inventory developed by David Street (http://www.cgrer.uiowa.edu/EMISSION_DATA_new/index_16.html). The biomass burning emissions were obtained from the Global Fire Emissions Database, Version 3 and have a monthly temporal resolution and 0.5 ° spatial resolution [van der Werf et al., 2010].

Fig. 1a illustrates the modelling domain which covered the entirety of East Asia (10.8 °N~59.6 °N, 51.9 °E~154.3 °E) with a horizontal grid interval of 36 km and 138×187 grid cells. This domain covered dust source regions over East Asia represented by erodibility in WRF-Chem model, as shown in Fig. 1b. The model atmosphere was divided into 35 vertical layers, and the model top pressure was 100 hPa. To reduce the computational time for the simulation, the integration period was 1st-23rd March 2010. Only the results from 18th-23rd March 2010 were used in this study (hereafter referred to as the simulation period). The meteorological initial and boundary conditions were constructed from the National Center for Environmental Prediction final analysis (NCEP/FNL) data at a

362 6-h temporal interval and 1 ° horizontal resolution. The NOAA land

363 surface model [Chen et al., 1996; Chen and Dudhia, 2001] and the Yonsei

364 University planetary boundary scheme [Hong, Noh and Dudhia, 2006]

365 were used in the simulation. The Morrison two-moment microphysics

366 scheme [Morrison et al., 2005] and Kain-Fritsch convective scheme

367 [Kain et al., 1990 and Kain et al., 2004] were also used to represent cloud

368 microphysics and convection processes [Zhao et al., 2013] in the

369 simulation. To produce a more realistic simulation of the large-scale

370 circulation situation and main weather systems, the modelled u- and v-

371 wind components and atmospheric temperatures were nudged towards the

372 NCEP/FNL analysis data with a nudging time scale of 6 h [Stauffer and

373 Seaman, 1990]. **3. Observations**

374 **3.1 CALIPSO Aerosol Extinction Coefficients**

375   The aerosol extinction profiles retrieved by the CALIPSO satellite

376 were used in the study. The CALIPSO satellite, launched in April 2006 to

377 investigate the vertical structure of aerosols and clouds, carries the Cloud-

378 Aerosol Lidar with Orthogonal Polarization (CALIOP) instrument

379 [Winker et al., 2006, 2007]. In this work, the observed aerosol extinction

380 from the CALIPSO level 2 5 km Cloud and Aerosol Profile Products

381 version 3.3 was analyzed. The retrievals were used to evaluate the

382 simulated vertical structure of dust particles along the orbital path at

383 20:08 UTC on 19th March 2010 in the study. The data for clouds and

384 stratospheric features by the atmospheric volume description and cloud

385 aerosol discrimination score was screened [Liu et al., 2004]. Features

386 with cloud aerosol discrimination scores exceeding 80 were selected for

387 this work, which provided a confidence for the classification of dust

388 layers using the CALIOP cloud-aerosol discrimination algorithm.

389 **3.2 Aerosol Robotic Network (AERONET) AOD**

390   AERONET is a global ground-based aerosol monitoring network

established by the National Aeronautics and Space Administration, and Photometry for Operational Satellite Processing Standards of the National Center for Scientific Research involves standardized automatic sun photometers that measure sun and sky radiances at several wavelengths in the visible and near-infrared bands. The observed radiances are further processed to retrieve aerosol properties via algorithms developed by Dubovik and King (2000) and Dubovik et al. (2002). Global aerosol optical depth is provided in near real time after calibration, processing and distribution. AOD data products are available at three levels based on data quality: unscreened data (Level 1.0), cloud-screened data (Level 1.5), and quality-assured and cloud screened data (Level 2.0). In this work, the level 2.0 products of AOD at SACOL, Mt. Waliguan (Mt_WLG), Taihu, Gwangju_GIST, Shirhuma and Ussuriysksites (Fig. 1a and Table 1) were used to evaluate the simulated AODs over the dust source regions and remote regions.

4. Results and discussions

4.1 Meteorological conditions

To evaluate the model performance in simulating dust emission and transport during the dust storm event, we first compared the simulated meteorological conditions against the reanalysis data and in situ measurements. The average wind and temperature fields at 500 hPa from the NCEP/FNL reanalysis data and WRF-Chem simulations over East Asia during the simulation period are shown in Fig. 2. Generally, WRF-Chem model reproduced the large-scale circulation field over East Asia extremely well, including the location and shape of the East Asian subtropical westerly jet stream, the lower-latitude edges of the westerly jet, and the upper-level westerly jet over East Asia (Fig. 2a). As to the wind speed, the WRF-Chem model was able to simulated it well over TD,

GD and eastern and southern China, where the differences with observation were only -0.6~0.6 m s^{-1}. The wind speed over the surrounding area of TD and TP was overestimated with the value of 1.2~3 m s^{-1} due to the complex terrain (Fig. 2b). The differences of temperature at 500 hPa between WRF-Chem model and NCEP/FNL reanalysis data over East Asia were also demonstrated in Fig. 2d. In general, the simulated temperature was almost consistent with the reanalysis data, especially in the eastern, southern and northwestern China. There were slightly underestimated values (-0.4~-0.6 ℃) over GD and extended to the surrounding areas of TD. Moreover, the WRF-Chem model can't simulate air temperature at 500 hPa over the TP well. The bias was up to -1.3℃ in the north slope of the TP that is beyond the scope of this study.

Wind rose diagrams for four meteorological stations including Tazhong over the TD and Guaizihu, Yumenzhen, and Mazongshan over the GD (Fig. 1a and Table 1) are shown in Fig. 3. The hourly 10-m wind observations were obtained from the Chinese National Meteorological Center and will be referred to as observed wind direction and wind speed records. The winds mainly blowed from west to east at the Tazhong site during the dust event. The wind speeds generally exceeded 2 m s^{-1}. The frequency of calm winds accounted for 8.0% of total wind records. The average magnitude of the observed wind speed at the Tazhong site (3.4 m s^{-1}) was lower than the average value of the simulations (5.2 m s^{-1}). Over the GD, the wind speeds were primarily between 3-10 m s^{-1}. The average wind speed exceeded that at the Tazhong site. At the Guaizihu site，the prevailing wind direction was from the west and the northwest. The simulated wind speed was slightly higher than the observed wind speed. At the Yumenzhen site，the prevailing wind direction was generally from

the east. The simulated wind speed (6.4 m s^{-1}) was higher than the observed wind speed (4.7 m s^{-1}). The Mazongshan site is west of the Guaizihu site. At this site the simulations did not capture the easterly component of the winds well.

Generally, WRF-Chem simulations reproduced the wind field at the surface in the dust source regions. However, the simulated wind speed at 10 m (4.2 m s^{-1} over the TD and 6.4 m s^{-1} over the GD) was slightly higher than the observed wind speed (3.5 m s^{-1} over the TD and 5.7 m s^{-1}). In addition, the frequency of calm winds in Tazhong and Guaizihu was 8.0% and 0.5%, respectively. The simulation results did not describe the calm winds well in these regions. It should be noted that the different frequencies of wind speed and direction between the observational records and numerical model might have contributed to the deviations in the results. Chen et al. (2014a) have analyzed the monthly averages of the 10-m winds over the TD and GD from observations, reanalysis data, and WRF-Chem simulations during 2007-2011. They also found that the WRF-Chem model could reproduce the observed seasonal and inter-annual variations of wind field over the TD and GD. However, the simulations misestimated the observed wind speed because of WRF model limitations in representing sub-grid variations and turbulence processes in the complex terrain and land surface types [Hanna et al., 2000]. This is a common issue in WRF simulations, which will be improved in a newer version of the WRF model through the use of surface drag parameterization [Chen et al., 2014; Jiménez and Dudhia, 2012]. Although simulations overestimate the magnitude of observed 10-m wind speed over the TD and GD, it could reproduce the observed spatial distribution of 10-m wind speed in dust source regions. Therefore, we could tune the value of the empirical proportionality constant C in the

475 GOCART dust emission schemes to keep the magnitude of modeled AOD
476 consistent with the observational data.

4.2 Spatial and temporal distribution of dust

478   The modelled dust optical properties were compared with those from
479 surface observation reports and satellite retrievals to validate WRF-Chem
480 model results. Fig. 4 shows spatial distributions of daily mean 550 nm
481 AOD from MODIS and the corresponding WRF-Chem simulations over
482 East Asia. The time series of the observed and modelled AODs at the six
483 AERONET sites (SACOL, Taihu, Mt_WLG, Ussuriysk, Gwangju_GIST,
484 and Shirahama in Fig. 1a and Table 2) are shown in Fig. 5. In addition,
485 the vertical profile of dust aerosols is the critical factor that determines
486 radiative forcing and climate response from mineral dust [Huang et al.,
487 2008]. The accurate estimates of the vertical structure make sense to
488 reveal the variation of the dust optical properties and dust long-term
489 transport mechanism. Cross-sections of aerosol extinction coefficients at
490 532 nm over the TD at 20:08 UTC (2:08 LT) on 19th March 2010 from
491 the WRF-Chem model and CALIPSO retrievals is shown in Fig. 6.

492   Generally, MODIS retrievals could be compared to the simulated AOD
493 over East Asia, although datasets were not insufficient because of their
494 limited spatial and temporal coverage. The modelling results generally
495 captured the observed AODs from the MODIS retrievals over the dust
496 source region, indicating that the GOCART dust emissions represented
497 the dust source function over East Asia well. The average MODIS AOD
498 and simulated AODs over the TD and GD were 0.88 and 0.82,
499 respectively. However, the simulated AOD was lower than the MODIS
500 AOD in the southwestern part of the domain, probably because of the
501 anthropogenic emissions in northern India were underestimated in the

18

502   simulation (Fig. 4).

503   The peak value center of the dust aerosol occurred in the TD and GD

504 and declined toward the north on 18th March (Fig. 4). The daily average

505 of the observed AOD at SACOL was 0.28, and the corresponding

506 simulated AOD was less than 0.1. Over dust remote regions, the dust

507 AOD accounted for less than 10% of the total AOD. Then, a large amount

508 of dust aerosol was injected, especially over the GD on 19th March. The

509 simulated AODs showed good consistency with those from the ground-

510 based data (Fig. 4). The dust AOD accounted for more than 95% of total

511 AOD at SACOL. The observed AOD was 0.58, which was comparable to

512 the corresponding simulated AOD (0.53) at SACOL.

513   The observed AOD over the TD exceeded that over the GD by 0.3

514 on 20th March. The simulated AODs over the GD underestimated the

515 MODIS AODs by up to 0.2 (Fig. 4). The observed AODs at SACOL were

516 higher than the simulated AOD by up to 15% because of the effects of the

517 local emission source. The AODs at SACOL and Mt_Waliguan AOD

518 showed a decreasing trend. However, the dust AODs began to increase at

519 the Taihu, Ussuriysk, and Gwangju_GIST sites, thus indicating that the

520 dust particles from the dust source regions were transported to Japan,

521 Korea, and Russia. The Mt_Waliguan AOD increased rapidly up to 0.5,

522 and the higher dust AOD (0.6±0.14) persisted at the Taihu site on 21st

523 March. On 22nd-23rd March, the TD and GD dust mass loadings greatly

524 weakened. The dust AODs were close to 0, except for the SACOL and

525 Mt_Waliguan sites, which are near the dust source regions (Fig. 45).

526   Moreover, WRF-Chem model captured the vertical structure of

527 aerosols over and near the TD well (Fig. 6). As is well known, the vertical

528 structure of mineral dust plays an important role in the atmospheric

529 heating rate [Minnis and Cox, 1978; Carlson and Benjamin, 1980], long-

530 wave radiative forcing in clear sky, and short-wave radiative forcing in

531 cloudy sky [Liao and Seinfeld, 1998; Meloni et al., 2005], thereby

532 directly affecting climate systems through changes in cloud height, cloud

533 life and precipitation because of the changes in the radiative balance.

534 Therefore, accurate estimates of the vertical structure can reasonably be

535 used to reveal variations in dust optical properties and long-term dust

536 transport mechanisms.

537 **4.3 Dust emission and transport**

538 The detailed dynamic processes of the strong dust storm event along

539 with the synoptic situation are discussed in the section. The simulation

540 domain was relatively small (Fig. 1a) and the characteristics of the larger

541 scale changes in the atmospheric circulation are not reflected in this

542 discussion. The spatial distributions of the geopotential heights,

543 temperatures and wind circulation at 500 hPa and 850 hPa from the

544 NCEP/FNL reanalysis data are shown in Figs. 7 and 8.

545 The dust storm was initialized by a cold air intrusion in the northern

546 part of Xinjiang on 18th March. The dense isotherm gradient led to the

547 stronger cold advection. A mass of cold air accumulated in the northern

548 part of the Tianshan Mountains, which decreased the surface

549 temperatures in northern China. The northwest flow along the Tianshan

550 Mountain was then injected into the TD deserts (Figs. 7 and 8). The

551 convergence of the warm and cold air led to the low level convergence,

552 which created dynamic conditions for the TD dust emission. The GD was

553 located in the warmer zone in advance of the cold front, which generated

554 uplift movement and further injected dust particles over the GD (Figs. 7

555 and 8). The dust layer over the GD accumulated at 850 hPa. The

maximum of $PM_{2.5}$ dust concentration reached 41 µg m^{-3} (Fig. 10). The daily average of the dust emission fluxes over the TD and GD were 20 and 28 µg m^{-2} s^{-1}, respectively (Fig. 9). This result was also consistent with Zhao et al. (2005) and Zhang et al. (2009). Zhao et al. (2005) pointed out that the dust emission over East Asia was about 18 µg m^{-2} s^{-1} in April and 15 µg m^{-2} s^{-1} in May using Northern Aerosol Regional Climate Model. Zhang et al. (2009) calculated the dust emission from 1997 to 2006 and the dust emission of TD along with the surround region was around 23 µg m^{-2} s^{-1} based on the Regional Climate Model RegCM version 3.

Dust emission over GD and TD had reached a maximum on 19th March for the dust event. The stronger cold advection greatly enhanced the atmospheric baroclinicity because the isotherm was almost perpendicular to the isoheight behind the trough. This context aided in the downward transport of momentum produced by the northwest flow in the high levels, which caused the strong wind and dust emissions (Figs. 7 and 8). The $PM_{2.5}$ dust concentrations over the TD reached up to 65 µg m^{-3} (Fig. 10). The GD dust particles were then transported long distances to eastern and southern China because of the high-level northwest flow. Thus, the PM2.5 dust concentrations in downwind regions including Korean Peninsula and Japan increased from 5 to 14 µg m^{-3} at 850 hPa. Cold air climbing over the Tianshan Mountain and joining with the strong northeast cold air over the TD caused a strong northwest wind, which enhanced dust emission over the TD. However, the height of dust layer over the TD (about 2 km) was lower than over the GD (about 4 km) (Fig. 10).

The cold advection behind the trough helped the cold vortex to spread slowly eastwards when the angle between the isotherm and the isoheight was sufficient on 20th March (Fig. 7). Cold air accumulated to the north of the Tianshan Mountains and then climbed over the mountains, spreading northwestwards (Fig. 8). The dust emission over the TD (18.4 μg m^{-2} s^{-1}) was further enhanced by the influence of the anticyclone behind the cold front. As the upper troughs weakened and moved out, the GD dust emission (8.2 μg m^{-2} s^{-1}) began to decrease (Fig. 9). The PM$_{2.5}$ dust concentration decreased to 22±8.2 μg m^{-3} (Fig. 10), thus indicating that the first stage of the dust storm event was essentially completes. The PM$_{2.5}$ dust concentration in eastern China and Korean Peninsula still increased and the maximum value was 26 μg m^{-3}. Dust particles in these downwind regions could reduce visibility, change radiative budget, and further modify atmospheric stability at regional scale [Chen et al. 2014; Kang, et al, 2013].

The period of 21st-23rd March is regarded as the second stage of the dust event. The TD dust emission peaked in this dust storm event on 21st March. The average TD dust emission flux was 37.2±6.4 μg m^{-2} s^{-1} (Fig. 9). The frontal zone in the upper atmosphere gradually moved south to north of 40 N (Fig. 7). Cold air climbed over the Pamir Plateau and intruded into the Tarim basin, which caused strong uplift motion over the TD. The TD dust particles accompanied by the jet stream and cold advection were transported to the most of northern China. However, the strength of the dust emission in this stage was weaker than that on 19th March. The strengthening of the frontal zones gradually decreased and the descending motions typically occurred over a larger area on 22nd-23rd March (Fig. 8). The dust emission flux decreased to 10 μg m^{-2} s^{-1} in the two dust source regions (Fig. 9). Moreover, the prevailing wind is the key

factor for producing significant differences in dust emission and long-term transport over the TD and GD (Fig. 11). The TD is located in the basin surrounded on three sides by mountains. And the wind at the low level over the TD is the East wind based. Therefore, TD dust is not easily transported out of the basin, although the TD has the largest dust emission in the second stage of the dust storm event. Compared to the TD, the GD is relatively flat areas. And the strong westerly wind over the GD is advantageous for ejecting and further transporting of GD dust. Sun et al. (2001) have also noted that GD dust can be entrained to an elevation of only <3 km in most cases (about 90%). The relatively lower-elevation dust layers are deposited mainly in inland China.

From the thermodynamic perspective, the GD dust was also more favorable than the TD dust in terms of the dust emission and vertical transport (Fig. 12). Specifically, the temperature profile over the GD from the surface to the 700 hPa was almost parallel to the dry adiabatic rate, indicating that the layer was in an absolutely unstable state, favoring of emission and vertical transport of the GD dust particles. In contrast, the sounding data in the TD revealed an unstable layer quite near the surface that ranged from the surface to a few hundred meters, helping to vertically elevate the TD dust. Nonetheless, the temperature lapse rate decreases with increasing altitude and is less than that in the wet adiabatic rate, indicating the existence an absolutely stable layer and thus requiring more energy to lift an air parcel. Therefore, the vertical movement of the air was inhibited, and the elevation of the dust layer ceased. In addition, the relative humidity in the GD was low within the entire layer, whereas it remained low in the TD in the lower-middle troposphere but increased with height, resulting in a humidity condition that was dryer below and

637   wetter above. This is the hallmark of a conditional stable state, which

638   inhibits the convective movement of the atmosphere.

4.4 Dust budget analysis

640   To better understand the relative contribution of dust emissions over

641   the TD and GD during the dust storm event, Fig. 13 shows that the

642   budgets for dust emission, transport, and dry and wet depositions over

643   the TD and GD, respectively. The positive sign represents increase to dust

644   concentration and the negative sign represents decrease to dust

645   concentration. Among the four budget terms, the source term of the dust

646   concentration was the absolute dust emission for the entire dust storm

647   event over the TD and GD. Emission contribution is absolute positive.

648   While dry/wet depositions as well as transport are sinks of dust in the

649   atmosphere, these values are always negative. Dry deposition is the

650   largest sink of dust, following by transport and wet deposition.

651   Specifically, the GD dust emission was the largest contributor to

652   dust concentration over East Asia in the first stage (18th-20th March) (Fig.

653   13). The daily dust emission flux over the GD peaked above 68 μg m^{-2} s^{-1}

654   (Fig. 9). The contribution of the transport of the GD dust particles (up to

655   3.4 ton day^{-1}) was much greater than that of the TD dust (up to 1.5 ton

656   day^{-1}) (Fig. 13). Therefore, more GD dust particles could have been

657   transported over East Asia. The strengthening dust emissions weakened

658   substantially in the second stage (21st-23rd March). The TD dust emission

659   exerted an important effect on dust concentrations in that stage. The

660   average TD dust emission flux was 20±4.6 μg m^{-2} s^{-1} (Fig. 9). However,

661   the transport capability of the GD dust was still stronger than that of the

662   TD dust in this stage. In Fig. 14, we can find that the GD dust particles

663   were accumulated under 3 km between 286 K-296 K. The GD dust

664   concentration reached up to 1500 μg m^{-3} (Fig. 14). The mass

concentrations of the TD dust in the lower-middle troposphere were lower than that of the GD dust.

4.5 Direct Radiative forcing induced by dust over East Asia

Dust significantly affected radiation budget over East Asia during the dust storm event. The simulation with and without dust particles was used to estimate the magnitude of dust radiative forcing in the study. The shortwave (SW), longwave (LW) and net (SW+LW) direct radiative forcing of dust aerosols at all-sky conditions are calculated at the top of the atmosphere (TOA), surface (SUR) and in the atmosphere (ATM) during the simulation period in Fig. 15. The spatial distribution of dust radiative forcing was similar to that of dust mass loading over East Asia with highest values over the TD and GD. The SW forcing induced by dust at the TOA over East Asia was generally negative with greatest values of -6 to -8 W m^{-2} and -2 to -4 W m^{-2} over the GD and TD, respectively. Compared with dust aerosol over the Sahara desert, East Asian dust has a complex refractive index with small imaginary part and the back scattering of dust particles is relatively strong, which lead to the high negative values of SW radiation forcing at the TOA [Wang et al., 2004; Jin et al., 2015]. The magnitude of direct radiative forcing at the TOA was dominated by the SW radiative forcing because the LW radiative forcing induced by dust was much smaller (0~1 W m^{-2}). The maximum net radiative forcing value at the TOA reached -10 W m^{-2} in southern Inner Mongolia, larger than over the TD (-5 W m^{-2}), which was consistent with the conclusion of Chen et al. (2014) with the values of -8.3 W m^{-2} and -5.2 W m^{-2} over the GD and TD, respectively.

The SW cooling effect of the dust was predominant at the surface exceeding -8 W m^{-2} in northern China, which was much stronger than the

LW warming effect (+2 to +8 W m^{-2}). The region of significant LW radiative forcing occurred mainly over the TD and GD while the SW radiative forcing almost covered the whole northern China with a higher value. As a result, the dust caused a strong cooling effect at the surface since dust aerosols weakened the incoming radiation through absorption and scattering of dust particles [Kumar et al., 2014; Jin et al., 2015]. The maximum net radiative forcing at the surface was as great as -14 W m^{-2} over the GD and -9.2 W m^{-2} along the dust transport pathway from northern China to Japan and Korean Peninsula, which is similar to the conclusions of Zhang et al (2009).

In the atmosphere, the dust aerosol induced positive SW radiative forcing (+1 to +11 W m^{-2}) and negative LW radiative forcing (-1 to -9 W m^{-2}), which led to warming in the atmosphere because of dust absorption. The LW radiative forcing was negative in TD and GD since the dust layers sent LW to TOA. The slightly positive net forcing varied from +4 to +8 W m^{-2} over the TD, +3 to +6 W m^{-2} over the GD, and 0 to +4 Wm^{-2} over eastern China, which showed the warming effect of dust layers in the atmosphere. The average net dust radiative forcing in the atmosphere varied from +1 to +6 W m^{-2} over the downwind regions, including eastern China, Korea and Japan. Therefore, the radiative heating rate of dust has a significant influence on the vertical distribution of temperature of atmosphere. Fig. 16 further illustrated that the vertical profiles of the radiative heating rate induced by dust particles over East Asia. In general, dust induced warming in the atmosphere, especially over the TD and GD. The radiative heating rate was maximum over the GD at 0.14±0.03 K day^{-1} in the 1~3 km layers, where the dust mass loading was greatest, and gradually decreased with height. In comparison, the radiative heating rate

719   peaked in the 1~2 km layers over the TD, exhibiting values ranging from

720   0.04 to 0.12 K day^{-1}, lower than those of the GD.

5. Summary

722   The WRF-Chem model was used to investigate a typical dust storm

723   event that occurred from 18th to 23rd March 2010 in the study. WRF-

724   Chem model is capable of simulating East Asian dust during the

725   simulation period. The spatial and temporal variations of large-scale

726   circulation field and dust aerosols over East Asia were captured by the

727   model. The evaluations provided confidence for further understanding the

728   emission and transport of the TD and GD dust over East Asia based on

729   the simulated results. The results showed that the weather conditions,

730   topographies and surface type of GD and TD are quite different, which

731   may lead to the difference of the dust emission, uplifted height, horizontal

732   and vertical dust flux and long distance transport. The GD dust

733   contributed significantly to the dust concentration over East Asia,

734   especially on 19th March. The GD was located in the warm zone in

735   advance of a cold front. Rapidly warming surface temperatures and cold

736   air advection at high levels caused strong instability in the atmosphere

737   which strengthened the downward momentum transported from the

738   middle and low troposphere and caused strong surface winds and gusts.

739   The ascending motion and strong surface winds provided the energy

740   needed for dust resuspension, lifting and transport over the GD.

741   Moreover, the GD is located at the relatively flat and high altitude regions

742   under the influence of and confluence of the northern and southern

743   westerly winds. Therefore, the GD dust particles were easily lofted to 4

744   km and transported eastward over Japan and Korean Peninsula. The

745   contribution of transport of the GD dust particles (up to 3.7 ton day^{-1}) was

746   much greater than of the TD dust (up to 0.8 ton day^{-1}) over East Asia in

747 the simulation period.

748   The TD dust was not easily transported out of the basin because of
749 the complex terrain and the prevailing wind, even if the TD has the larger
750 dust emission. Specifically, the TD is surrounded by mountain ranges that
751 exceed 3 km in height, except for the Hexi corridor opening to the
752 northeast. The process that generated the dust storms was strongly
753 affected by these topographical characteristics in addition to the surface
754 conditions. In addition, the easterly wind dominated the TD areas. Thus,
755 the contribution of the transported TD dust to the dust sink was still
756 smaller than that of the GD dust. However, a small amount of finer dust
757 particles over the TD ($PM_{2.5}$ dust concentration was approximately 8.7 ug
758 m^{-3}) was lifted to 4 km or higher, which were transported long distances
759 from the source regions. The effects of the TD dust were not only local
760 but worked on regions far from the sources as well.

761   East Asian dust during the dust storm event plays a role in the
762 radiation budget. Generally, compared with previous modeling estimates
763 of direct radiative forcing by dust over East Asia, our estimates are
764 comparable with these modeling studies [Zhang et al., 2009; Han et al.,
765 2012; Chen et al., 2014; Conant et al., 2003; Park et al.,2005]. The net
766 dust radiative forcing over the East Asia was about -6.5 W m^{-2}(-8.4 W m^{-2}
767) at the TOA (surface) in this study, which is similar to the estimates
768 given by Conant et al. (2003) and Park et al. (2005), about -5 and -8 W m^{-2}
769 (-6 and -11 W m^{-2}) at the TOA (surface), respectively. However, the
770 uncertainties in direct radiative forcing over East Asia are still existed.
771 The biases in estimates of direct radiative forcing in simulations could be
772 attributed to following reasons. First of all, biases from dust emission
773 scheme, dust transport and deposition scheme could greatly affect the
774 assessments of dust radiative forcing in the model. Moreover, differences

775 in the vertical distribution of dust layer, dust particle size distribution, and
776 absorptive characteristics and meteorological conditions could influence
777 on the large differences in the quantitative assessment of dust radiative
778 forcing [Tegen et al., 1996; H Wang et al., 2004, 2007; Wu et al., 2004].

779 Overall, compared with the TD dust, the importance of the GD dust
780 to dust concentration in eastern China, Japan and Korea is most often
781 neglected. Our study focused primarily on the dynamics and
782 thermodynamics of dust emission and transport over TD and GD and
783 further elucidated the influence of TD and GD dust on the entire East
784 Asia based on a case study using the WRF-Chem model. However, it is
785 necessary to further investigate the quantitative contributions of TD and
786 GD dust for the dust mass concentrations over East Asia for a longer time
787 scale based on sensitivity tests in numerical model. In addition, the
788 climate effects of the GD dust over East Asia are needed to investigate in
789 the future.

790

797

798 **References:**

799 Ackermann, I. J., Hass, H., Memmesheimer, M., Ebel, A., Binkowski, F. S., and Shankar, U.:
800 Modal aerosol dynamics model for Europe, Atmos. Environ., 32, 2981–2999,
801 doi:10.1016/S1352-2310(98)00006-5, 1998.
802 Barnard, J. C., Fast, J. D., Paredes-Miranda, G., Arnott, W. P., and Laskin, A.: Technical Note:
803 Evaluation of the WRF-Chem "Aerosol Chemical to Aerosol Optical Properties" Module
804 using data from the MILAGRO campaign, Atmos. Chem. Phys., 10, 7325–7340,

805   doi:10.5194/acp-10-7325-2010, 2010.

806   Bi, J., Huang, J., Fu, Q., Wang, X., Shi, J., Zhang, W., Huang, Z., Zhang, B.: Toward
807   characterization of the aerosol optical properties over Loess Plateau of Northwestern
808   China. Journal of Quantitative Spectroscopy & Radiative Transfer, 112(2):346-360, doi:
809   10.1016/j.jqsrt.2010.09.006, 2011.

810   Carlson, T. N. and Benjamin, S. G.: Radiative Heating Rates for Saharan Dust, J. Atmos. Sci.,
811   37, 193–213, doi:10.1175/1520-0469(1980)037<0193:RHRFSD>2.0.CO;2, 1980.

812   Chen, F. and Dudhia, J.: Coupling an Advanced Land Surface–Hydrology Model with the
813   Penn State–NCAR MM5 Modeling System. Part I: Model Implementation and
814   Sensitivity, Mon. Weather Rev., 129, 569–585, doi:10.1175/1520-
815   0493(2001)129<0569:CAALSH>2.0.CO;2, 2001.

816   Chen, F., Mitchell, K., Schaake, J., Xue, Y., Pan, H. L., Koren, V., Duan, Q. Y., Ek, M., and
817   Betts, A.: Modeling of land surface evaporation by four schemes and comparison with
818   FIFE observations, J. Geophys. Res. Atmos., 101(D3), 7251–7268, doi:
819   10.1029/95JD02165, 1996.

820   Chen, S., Zhao, C., Qian, Y., Leung, Ruby, L., Huang, J., Huang, Z, W., Bi, J, R., Zhang, W.,
821   Shi, J., Yang, L., Li, D., Li, J. : Regional modeling of dust mass balance and radiative
822   forcing over East Asia using WRF-Chem, Aeolian Research.,15,15-30,
823   doi:10.1016/j.aeolia.2014.02.001, 2014.

824   Chen, S., Huang, J., Zhao, C., Qian, Y., Leung, L. R., and Yang, B.: Modeling the transport
825   and radiative forcing of Taklimakan dust over the Tibetan Plateau: A case study in the
826   summer of 2006, J. Geophys. Res. Atmos., 118, 797–812, doi:10.1002/jgrd.50122, 2013.

827   Chen, S., Zhao, C., Qian, Y., Leung, L. R., Huang, J., Huang, Z., Bi, J., Zhang, W., Shi, J.,
828   Yang, L., Li, D., and Li, J.: Regional modeling of dust mass balance and radiative
829   forcing over East Asia using WRF-Chem, Aeolian Res., 15, 15–30,
830   doi:10.1016/j.aeolia.2014.02.001, 2014.

831   Chen, S., Huang, J., Qian, Y., Ge, J., and Su, J.: Effects of aerosols on autumn precipitation
832   over Mid-Eastern China, J. Trop. Meteorol., 20, 242–250, 2014.

833   Dubovik, O. and King, M. D.: A flexible inversion algorithm for retrieval of aerosol optical
834   properties from Sun and sky radiance measurements, J. Geophys. Res. Atmos.,
835   105(D16), 20673–20696, doi: 10.1029/2000JD900282, 2000.

836   Dubovik, O., Holben, B., Eck, T. F., Smirnov, A., Kaufman, Y. J., King, M. D., Tanré, D., and
837   Slutsker, I.: Variability of Absorption and Optical Properties of Key Aerosol Types
838   Observed in Worldwide Locations, J. Atmos. Sci., 59, 590–608, doi:10.1175/1520-
839   0469(2002)059<0590:VOAAOP>2.0.CO;2, 2002.

840   Eguchi, K., Uno, I., Yumimoto, K., Takemura, T., Shimizu, A., Sugimoto, N., and Liu, Z.:
841   Trans-pacific dust transport: integrated analysis of NASA/CALIPSO and a global

842 aerosol transport model, Atmos. Chem. Phys., 9, 3137–3145, doi:10.5194/acp-9-3137-
843   2009, 2009.

844 Fu, Q., Thorsen, T J., Su, J., Ge, J., Huang, J.: Test of Mie-based single-scattering properties
845   of non-spherical dust aerosols in radiative flux calculations. Journal of Quantitative
846   Spectroscopy & Radiative Transfer, 110(14–16):1640-1653, doi:
847   10.1016/j.jqsrt.2009.03.010, 2009

848 Ginoux, P., Chin, M., Tegen, I., Prospero, J. M., Holben, B., Dubovik, O., and Lin, S. J.:
849   Sources and distributions of dust aerosols simulated with the GOCART model, J.
850   Geophys. Res., 106(D17), 20255, doi: 10.1029/2000JD000053, 2001.

851 Grell, G. A., Peckham, S. E., Schmitz, R., McKeen, S. A., Frost, G., Skamarock, W. C., and
852   Eder, B.: Fully coupled "online" chemistry within the WRF model, Atmos. Environ., 39,
853   6957–6975, doi:10.1016/j.atmosenv.2005.04.027, 2005..

854 Ge, J., J., Huang, C., Xu, Y., Qi, and H., Liu: Characteristics of Taklimakan dust emission
855   and distribution: A satellite and reanalysis field perspective. Journal of Geophysical
856   Research: Atmospheres, 119, 11,772–11,783, doi:10.1002/2014JD022280, 2014.

857 Han, Z., Li, J., Xia, X., Zhang, R.: Investigation of direct radiative effects of aerosols in dust
858   storm season over East Asia with an online coupled regional climate-chemistry-aerosol
859   model, Atmos. Environ.,54,688-699, doi:10.1016/j.atmosenv.2012.01.041,2012.

860 Hanna, S. R., Yang, R., and Yin, X.: Evaluations of numerical weather prediction (NWP)
861   models from the point of view of inputs required by atmospheric dispersion models, Int.
862   J. Environ. Pollut., 14, 98–105, doi:10.1504/IJEP.2000.000530, 2000.

863 Hong, S. Y., Noh, Y., and Dudhia, J.: A New Vertical Diffusion Package with an Explicit
864   Treatment of Entrainment Processes, Mon. Weather Rev., 134, 2318–2341,
865   doi:10.1175/MWR3199.1, 2006.

866 Hsu, N. C., Tsay, S. C., King, M. D., and Herman, J. R.: Deep Blue Retrievals of Asian
867   Aerosol Properties during ACE-Asia, IEEE Trans. Geosci. Remote Sens., 44, 3180–
868   3195, doi:10.1109/TGRS.2006.879540, 2006.

869 Huang, J., Lin, B., Minnis, P., Wang, T., Wang, X., Hu, Y., Yi, Y., and Ayers, J. K.: Satellite-
870   based assessment of possible dust aerosols semi-direct effect on cloud water path over
871   East Asia, Geophys. Res. Lett., 33, L19802, doi:10.1029/2006GL026561, 2006a.

872 Huang, J., Wang, Y., Wang, T., and Yi, Y.: Dusty cloud radiative forcing derived from satellite
873   data for middle latitude regions of East Asia, Prog. Nat. Sci., 16, 1084–1089,
874   doi:10.1080/10020070612330114,2006b.

875 Huang, J., Minnis, P., Lin, B., Wang, T., Yi, Y., Hu, Y., Sun-Mack, S., and Ayers, K.: Possible
876   influences of Asian dust aerosols on cloud properties and radiative forcing observed
877   from MODIS and CERES, Geophys. Res. Lett., 33, L06824,
878   doi:10.1029/2005GL024724, 2006c.

879 Huang, J., Minnis, P., Yi, Y., Tang, Q., Wang, X., Hu, Y., Liu, Z., Ayers, K., Trepte, C., and
880 Winker, D.: Summer dust aerosols detected from CALIPSO over the Tibetan Plateau,
881 Geophys. Res. Lett., 34, L18805, doi:10.1029/2007GL029938, 2007.

882 Huang, J. P., Huang, Z. W., Bi, J. R., Zhang, W., and Zhang, L.: Micro-pulse lidar
883 measurements of aerosol vertical structure over the Loess Plateau, Atmos. Ocean. Sci.
884 Lett., 1, 8–11, doi:10.1080/16742834.2008.11446756, 2008a.

885 Huang, J., Minnis, P., Chen, B., Huang, Z., Liu, Z., Zhao, Q., Yi, Y., and Ayers, J. K.: Long-
886 range transport and vertical structure of Asian dust from CALIPSO and surface
887 measurements during PACDEX, J. Geophys. Res., 113(D23), D23212,
888 doi:10.1029/2008JD010620, 2008b.

889 Huang, J., Zhang, W., Zuo, J., Bi, J., Shi, J., Wang, X., Chang, Z., Huang, Z., Yang, S., Zhang,
890 B., Wang, G., Feng, G., Yuan, J., Zhang, L., Zuo, H., Wang, S., Fu, C., and Jifan, C.: An
891 overview of the Semi-arid Climate and Environment Research Observatory over the
892 Loess Plateau, Adv. Atmos. Sci., 25, 906–921, doi:10.1007/s00376-008-0906-7, 2008c.

893 Huang, J., Fu, Q., Su, J., Tang, Q., Minnis, P., Hu, Y., Yi, Y., and Zhao, Q.: Taklimakan dust
894 aerosol radiative heating derived from CALIPSO observations using the Fu-Liou
895 radiation model with CERES constraints, Atmos. Chem. Phys., 9, 4011–4021,
896 doi:10.5194/acp-9-4011-2009, 2009.

897 Huang, J., Minnis, P., Yan, H., Yi, Y., Chen, B., Zhang, L., and Ayers, J. K.: Dust aerosol
898 effect on semi-arid climate over Northwest China detected from A-Train satellite
899 measurements, Atmos. Chem. Phys., 10, 6863–6872, doi:10.5194/acp-10-6863-2010,
900 2010.

901 Huang, J., Fu, Q., Zhang, W., Wang, X., Zhang, R., Ye, H., and Warren, S. G.: Dust and Black
902 Carbon in Seasonal Snow Across Northern China, Bull. Am. Meteorol. Soc., 92, 175–
903 181, doi:10.1175/2010BAMS3064.1, 2011.

904 Huang, J., Guan, X., and Ji, F.: Enhanced cold-season warming in semi-arid regions, Atmos.
905 Chem. Phys., 12(, 5391–5398, doi:10.5194/acp-12-5391-2012, 2012.

906 Huang, J., Wang, T., Wang, W., Li, Z., and Yan, H.: Climate effects of dust aerosols over East
907 Asian arid and semiarid regions, J. Geophys. Res. Atmos., 119, 11,398–11,416,
908 doi:10.1002/2014JD021796, 2014.

909 Huang, J., Yu, H., Guan, X., Wang, G., and Guo, R.: Accelerated dryland expansion under
910 climate change, Nat. Clim. Chang., 6, 166–171 [online] Available from:
911 doi:10.1038/nclimate2837, 2016.

912 Huang, X. X., Wang, T. J., Jiang, F., Liao, J. B., Cai, Y. F., Yin, C. Q., Zhu, J. L., and Han, Y.:
913 Studies on a severe dust storm in East Asia and its impact on the air quality of Nanjing,
914 China, Aerosol Air Qual. Res., 13, 179–193, doi:10.4209/aaqr.2012.05.0108, 2013.

915 Huang, Z., Huang, J., Bi, J., Wang, G, Wang, W, Fu, Q., Li, Z., Tsay, S., Shi, J.: Dust aerosol

vertical structure measurements using three MPL lidars during 2008 China-U.S. joint dust field experiment. J. Geophys. Res. Atmos., 115(D7):1307-1314, doi: 10.1029/2009JD013273, 2010.

Jiménez, P. A. and Dudhia, J.: Improving the Representation of Resolved and Unresolved Topographic Effects on Surface Wind in the WRF Model, J. Appl. Meteorol. Climatol., 51, 300–316, doi:10.1175/JAMC-D-11-084.1, 2012.

Jin, Q., Wei, J., Yang, Z.-L., Pu, B., and Huang, J.: Consistent response of Indian summer monsoon to Middle East dust in observations and simulations, Atmos. Chem. Phys., 15, 9897-9915, doi: 10.5194/acp-15-9897-2015, 2015.

Kain, J. S.: The Kain–Fritsch Convective Parameterization: An Update, J. Appl. Meteorol., 43, 170–181, doi:10.1175/1520-0450(2004)043<0170:TKCPAU>2.0.CO;2, 2004.

Kain, J. S. and Fritsch, J. M.: A One-Dimensional Entraining/Detraining Plume Model and Its Application in Convective Parameterization, J. Atmos. Sci., 47, 2784–2802, doi:10.1175/1520-0469(1990)047<2784:AODEPM>2.0.CO;2, 1990.

Kaufman, Y. J., Wald, A. E., Remer, L. A., Gao, B. C., Li, R. R., and Flynn, L.: The MODIS 2.1-mm channel-correlation with visible reflectance for use in remote sensing of aerosol, IEEE Trans. Geosci. Remote Sens., 35, 1286–1298, doi:10.1109/36.628795, 1997.

Koren, I., Kaufman, Y. J., Remer, L. A., and Martins, J. V: Measurement of the effect of Amazon smoke on inhibition of cloud formation., Science, 303, 1342–1345, doi:10.1126/science.1089424, 2004.

Kurosaki, Y., and Mikami, M.: Threshold wind speed for dust emission in East Asia and its seasonal variations, J. Geophys. Res., 112, D17202, doi:10.1029/2006JD007988, 2007.

Li, Z., Li, C., Chen, H., Tsay, S. C., Holben, B., Huang, J., Li, B., Maring, H., Qian, Y., Shi, G., Xia, X., Yin, Y., Zheng, Y., and Zhuang, G.: East Asian Studies of Tropospheric Aerosols and their Impact on Regional Climate (EAST-AIRC): An overview, J. Geophys. Res., 116, D00K34, doi:10.1029/2010JD015257, 2011.

Li, J., Z., Wang, G., Zhuang, G., Luo, Y., Sun, and Q., Wang.: Mixing of Asian mineral dust with anthropogenic pollutants over East Asia: a model case study of a super-dust storm in March 2010. Atmos. Chem. Phys., 12, 7591–7607, doi:10.5194/acp-12-7591-2012, 2012.

Liao, H. and Seinfeld, J. H.: Radiative forcing by mineral dust aerosols: Sensitivity to key variables, J. Geophys. Res. Atmos., 103(D24), 31637–31645, doi:10.1029/1998JD200036, 1998.

Liu, Z., Vaughan, M. A., Winker, D. M., Hostetler, C. A., Poole, L. R., Hlavka, D., Hart, W. and McGill, M.: Use of probability distribution functions for discriminating between clouds and aerosol in lidar backscatter data, J. Geophys. Res. D Atmos., 109(15), doi:10.1029/2004JD004732, 2004.

953 Meloni, D., di Sarra, A., Di Iorio, T., and Fiocco, G.: Influence of the vertical profile of
954   Saharan dust on the visible direct radiative forcing, J. Quant. Spectrosc. Radiat.Transf.,
955   93, 397–413, doi:10.1016/j.jqsrt.2004.08.035, 2005.

956 Minnis, P. and Cox, S. K.: Magnitude of the radiative effects of the Sahara dust layer, Atmos.
957   Sci. Pap. 283, 111 pp., Colo. State Univ., Ft. Collins, Colo., 1978.

958 Morrison, H., Curry, J. A., and Khvorostyanov, V. I.: A New Double-Moment Microphysics
959   Parameterization for Application in Cloud and Climate Models. Part I: Description, J.
960   Atmos. Sci., 62, 1665–1677, doi:10.1175/JAS3446.1, 2005.

961 Martonchik, J. V., Diner, D. J., Crean, K., and Bull, M.: Regional aerosol retrieval results
962   from MISR, IEEE Trans. Geosci. Remt. Sensing., 40, 1520-1531, 2002.

963 Martonchik, J. V., Diner, D. J., Kahn, R. A., Gaitley, B. J., and Holben, B. N.: Comparison of
964   MISR and AERONET aerosol optical depths over desert sites, Geophys. Res. Let., 31,
965   L16102, doi:10.1029/2004GL019807, 2004.

966 Qian, Y., Gong, D., Fan, J., Leung, L. R., Bennartz, R., Chen, D., and Wang, W.: Heavy
967   pollution suppresses light rain in China: Observations and modeling, J. Geophys. Res.,
968   114(D7), D00K02, doi:10.1029/2008JD011575, 2009.

969 Ramanathan, V., Crutzen, P. J., Kiehl, J. T., and Rosenfeld, D.: Aerosols, climate, and the
970   hydrological cycle., Science, 294, 2119–24, doi:10.1126/science.1064034, 2001.

971 Rea, D. K.: The paleoclimatic record provided by eolian deposition in the deep sea: The
972   geologic history of wind, Rev. Geophys., 32, 159-195, doi:10.1029/93RG03257, 1994.

973 Shao, Y., Ishizuka, M., Mikami, M., and Leys, J. F.: Parameterization of size-resolved dust
974   emission and validation with measurements, J. Geophys. Res.,116,D08203,doi:
975   10.1029/2010JD014527, 2011.

976 Schell, B., Ackermann, I. J., Hass, H., Binkowski, F. S., and Ebel, A.: Modeling the formation
977   of secondary organic aerosol within a comprehensive air quality model system, J.
978   Geophys. Res. Atmos., 106(D22), 28275–28293, doi:10.1029/2001JD000384, 2001.

979 Stauffer, D. R. and Seaman, N. L.: Use of Four-Dimensional Data Assimilation in a Limited-
980   Area Mesoscale Model. Part I: Experiments with Synoptic-Scale Data, Mon. Weather
981   Rev., 118, 1250–1277, doi:10.1175/1520-0493(1990)118<1250:UOFDDA>2.0.CO;2,
982   1990.

983 Skamarock, W. C., Klemp, J. B., Dudhia, J., Gill, D. O., Baker, D. M., Duda, M. G., Huang,
984   X., Wang, W., and Powers, J. G.: A description of the Advanced Research WRF version
985   3:Mesoscale and Microscale Meteorology Division, National Center for Atmospheric
986   Research, Boulder, Colorado, USA, 113, 2008.

987 Su, J., Huang, J., Fu, Q., Minnis, P., Ge, J., and Bi, J.: Estimation of Asian dust aerosol effect
988   on cloud radiation forcing using Fu-Liou radiative model and CERES measurements,
989   Atmos. Chem. Phys., 8, 2763–2771, doi:10.5194/acp-8-2763-2008, 2008.

990 Sun, J., Zhang, M., and Liu, T.: Spatial and temporal characteristics of dust storms in China
991   and its surrounding regions, 1960-1999: Relations to source area and climate, J.
992   Geophys. Res. Atmos., 106(D10), 10325–10333, doi:10.1029/2000JD900665, 2001.

993 Takamura, T., T. Nakajima, and SKYNET community group: Overview of SKYNET and its
994   Activities. Opt. Pura y Apl., 37, 3303–3308, 2004

995 Takamura, T., N. Sugimoto, A. Shimizu, A. Uchiyama, A. Yamazaki, K. Aoki, T. Nakajima,
996   B. J. Sohn, and H. Takenaka.: Aerosol radiative characteristics at Gosan, Korea, during t
997   he atmospheric brown cloud East Asian regional experiment 2005. J. Geophys. Res., 112
998   , D22S36, doi:10.1029/2007JD008506, 2007.

999 Tsunematsu, N.: Observed dust storm in the Taklimakan Desert on April 13, 2002. Sci. Online
1000   Lett. Atmos., 1, 21–24,doi:10.2151/sola.2005-006,2005.

1001 Uno, I., Amano, H., Emori, S., Kinoshita, K.., Matsui, I., and Sugimoto, N.: Trans-Pacific
1002   yellow sand transport observed in April 1998: A numerical simulation, J. Geophys. Res.
1003   Atmos., 106(D16), 18331–18344, doi:10.1029/2000JD900748, 2001.

1004 van der Werf, G. R., Randerson, J. T., Giglio, L., Collatz, G. J., Mu, M., Kasibhatla, P. S.,
1005   Morton, D. C., DeFries, R. S., Jin, Y., and van Leeuwen, T. T.: Global fire emissions and
1006   the contribution of deforestation, savanna, forest, agricultural, and peat fires (1997–
1007   2009), Atmos. Chem. Phys., 10, 11707–11735, doi:10.5194/acp-10-11707-2010, 2010.

1008 Wang, H., Zhang, X. Y., Gong, S. L., Chen, Y., Shi G. Y., and Li, W.: Radiative feedback of
1009   dust aerosols on the East Asian dust storms, J. Geophys. Res., 115, D23214,
1010   doi:10.1029/2009JD013430, 2010.

1011 Wang, H., Shi, G. Y., Teruo, A., Wang, B., and Zhao, T. L.: Radiative forcing due to dust
1012   aerosol over east Asia-north Pacific region during spring 2001, Chin. Sci. Bull., 49,
1013   2212–2219, 2004.

1014 Wang, J., Xu, X., Henze, D K., Zeng, J., Ji, Q., Tsay, S., Huang, J.: Top-down estimate of dust
1015   emissions through integration of MODIS and MISR aerosol retrievals with the GEOS-
1016   Chem adjoint model. Geophys. Res. Lett., 39(8):142-148, doi: 10.1029/2012GL051136,
1017   2012.

1018 Wang, X., Huang, J., Zhang, R., Chen, B., Bi, J.: Surface measurement of aerosol properties
1019   over northwest China during ARM China 2008 deployment. J. Geophys. Res. Atmos.,
1020   115(11):2333-2338, doi: 10.1016/j.jqsrt.2010.09.006, 2010.

1021 Winker, D., Pelon, J., and Mc Cormick, M.: Initial results from CALIPSO, 23rd International
1022   Laser Radar Conference, Nara, Japan, 2006.

1023 Ye, H., R.Z., Zhang, J.S., Shi, J.P., Huang, S. W., Q. Fu: Black carbon in seasonal snow across
1024   northern Xinjiang in northwestern China, Environmental Research Letters, 7(4):044002,
1025   2012.

1026 Winker, D., Hunt, W., and Mc Gill, M.: Initial performance assessment of CALIOP,

1027   Geophys.Res. Lett., 34(19), doi:10.1029/2007GL030135, 2007.

1028 Zhang, Y., Takahashi, M., and Guo, L.: Analysis of the East Asian Subtropical Westerly Jet
1029   Simulated by CCSR/NIES/FRCGC Coupled Climate System Model, J. Meteorol. Soc.
1030   Japan. Ser. II, 86, 257–278, doi:10.2151/jmsj.86.257, 2008.

1031 Zhang, X. Y., Gong, S. L., Zhao, T. L., Arimoto, R., Wang, Y. Q., and Zhou, Z. J.: Sources of
1032   Asian dust and role of climate change versus desertification in Asian dust emission,
1033   Geophys. Res. Lett., 30, NO.24,2272,doi:10.1029/2003GL018206, 2003.

1034 Zhao, C., Chen, S., Leung, L. R., Qian, Y., Kok, J. F., Zaveri, R. A., and Huang, J.:
1035   Uncertainty in modeling dust mass balance and radiative forcing from size
1036   parameterization, Atmos. Chem. Phys., 13, 10733–10753, doi:10.5194/acp-13-10733-
1037   2013, 2013.

1038 Zhao, C., Liu, X., and Leung, L. R.: Impact of the Desert dust on the summer monsoon
1039   system over Southwestern North America, Atmos. Chem. Phys., 12, 3717–3731,
1040   doi:10.5194/acp-12-3717-2012, 2012.

1041 Zhao, C., Liu, X., Leung, L. R., Johnson, B., McFarlane, S. A., Gustafson, W. I., Fast, J. D.,
1042   and Easter, R.: The spatial distribution of mineral dust and its shortwave radiative
1043   forcing over North Africa: modeling sensitivities to dust emissions and aerosol size
1044   treatments, Atmos. Chem. Phys., 10, 8821–8838, doi:10.5194/acp-10-8821-2010, 2010.

1045 Zhao, C., Liu, X., Ruby Leung, L., and Hagos, S.: Radiative impact of mineral dust on
1046   monsoon precipitation variability over West Africa, Atmos. Chem. Phys., 11, 1879–1893,
1047   doi:10.5194/acp-11-1879-2011, 2011.

1048 Zhao, T. L., Gong, S. L., Zhang, X. Y., Blanchet, J. P., McKendry,I. G., and Zhou, Z. J.:A
1049   simulated climatology of Asian dust aerosol and its trans-Pacific transport. Part I: Mean
1050   climate and validation, J. Climate, 19, 88–103, 2006.

1051 Zhao, T. L., Gong, S. L., Zhang, X. Y., and Mckendry, I.G.:Modeled size-segregated wet and
1052   dry deposition budgets of soil dust aerosol during ACE-Asia 2001: Implications for
1053   trans-Pacific transport, J. Geophys. Res., 108, 8665, doi:10.1029/2002JD003363, 2003.

1054 Zhang, X.Y., Gong, S.L., Zhao, T.L., Arimoto, R., Wang, Y.Q., Zhou, Z.J.:Sources of Asian
1055   dust and role of climate change versus desertification in Asian dust emission. Geophys.
1056   Res. Lett. 30 (24), 2272, doi:10.1029/ 2003GL018206, 2003.

1057
1058
1059
1060
1061
1062
1063

1064 Table1 Information about the 10-m wind stations from the Chinese National
1065 Meteorological Center (CNMC)

Name	Latitude (°N)	Longitude (°E)	Elevation (m)
Tazhong	39.00	83.40	1099.3
Guaizihu	41.22	102.22	960.0
Yumenzhen	40.16	97.02	1527.0
Maoyinbadao	40.10	104.18	1325.9

1066
1067
1068
1069
1070
1071
1072
1073
1074 Table 2 Information about selected AERONET stations

Name	Latitude (°N)	Longitude (°E)	Elevation (m)
SACOL (China)	35.95	104.14	1965.8
Mt_Waliguan (China)	36.28	100.90	3816.0
Taihu (China)	31.42	120.22	20.0
Gwangju_GIST(Korea)	35.23	126.84	52.0
Shirhuma (Japan)	33.69	135.36	10.0
Ussuriysk(Russia)	43.70	132.16	280.0

1075
1076
1077
1078
1079
1080
1081
1082
1083
1084
1085
1086
1087
1088
1089
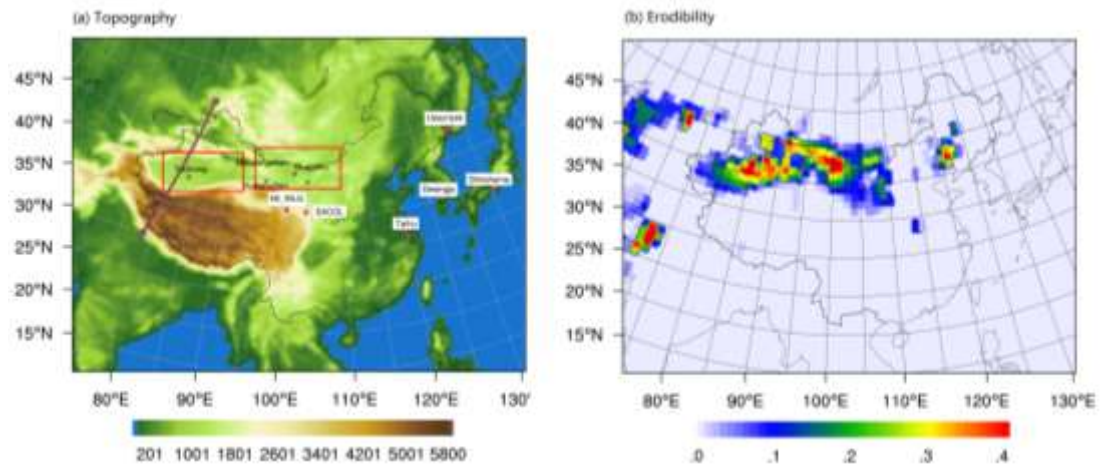
1090

Fig. 1 (a) Modelling domain and spatial distribution of the topography over East Asia. Taklimakan Desert (TD) and Gobi Desert (GD) are indicated by the red boxes. The pink dots are the AERONET sites (SACOL, Mt. Waliguan (Mt_WLG), Taihu, Gwangju_GIST, Shirhuma and Ussuriysk). The black stars are the sites with observed 10-m winds (Tazhong, Maozongshan, Yumenzhen, and Guaizihu). The blown line represents the orbit path of CALIPSO/CALIOP over the TD at 0:08 UTC (2:08 LT) on 19th March 2010. (b) Soil erodibility used in GOCART dust emission scheme from WRF-Chem model.
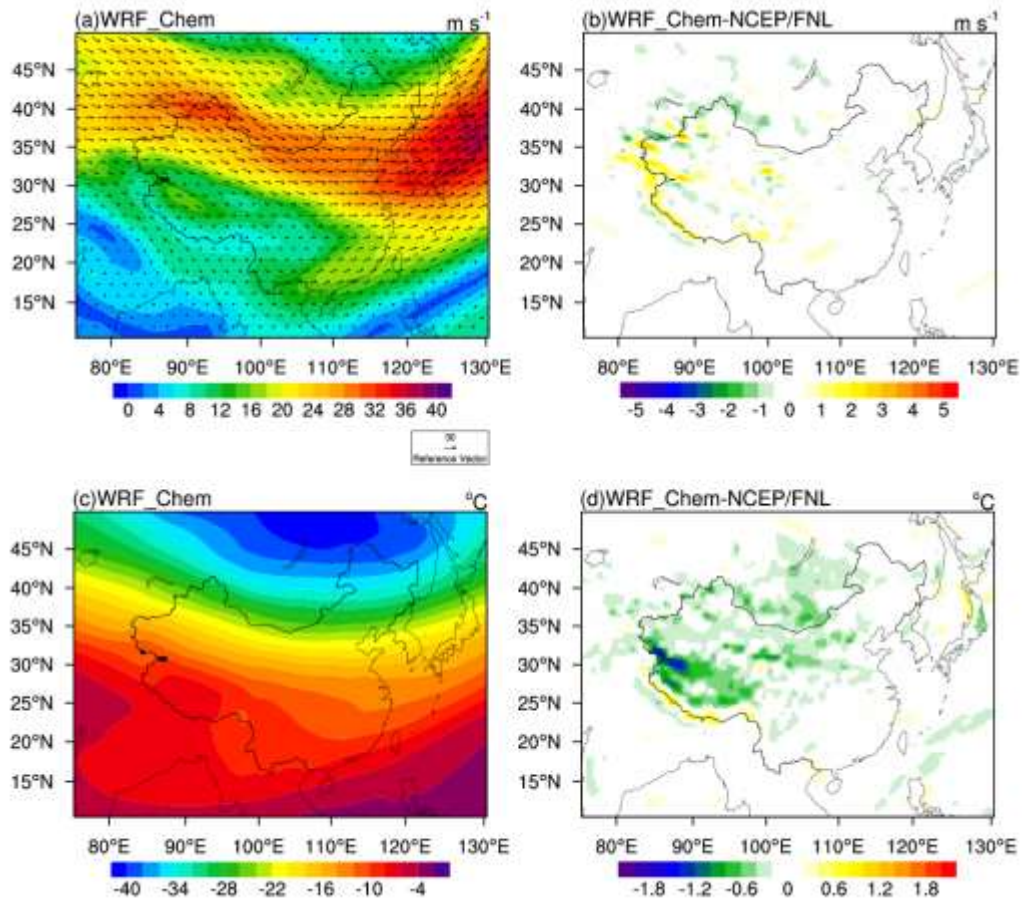
Fig.2 The simulated average wind (Fig. 2a) as well as temperature fields (Fig. 2c) at 500 hPa and the difference between the simulation and NCEP/FNL reanalysis data (Fig. 2b and Fig. 2d) over East Asia during March 18th to 23rd , 2010 (hereafter referred to the simulation period). Arrows represent wind vector at 500 hPa.
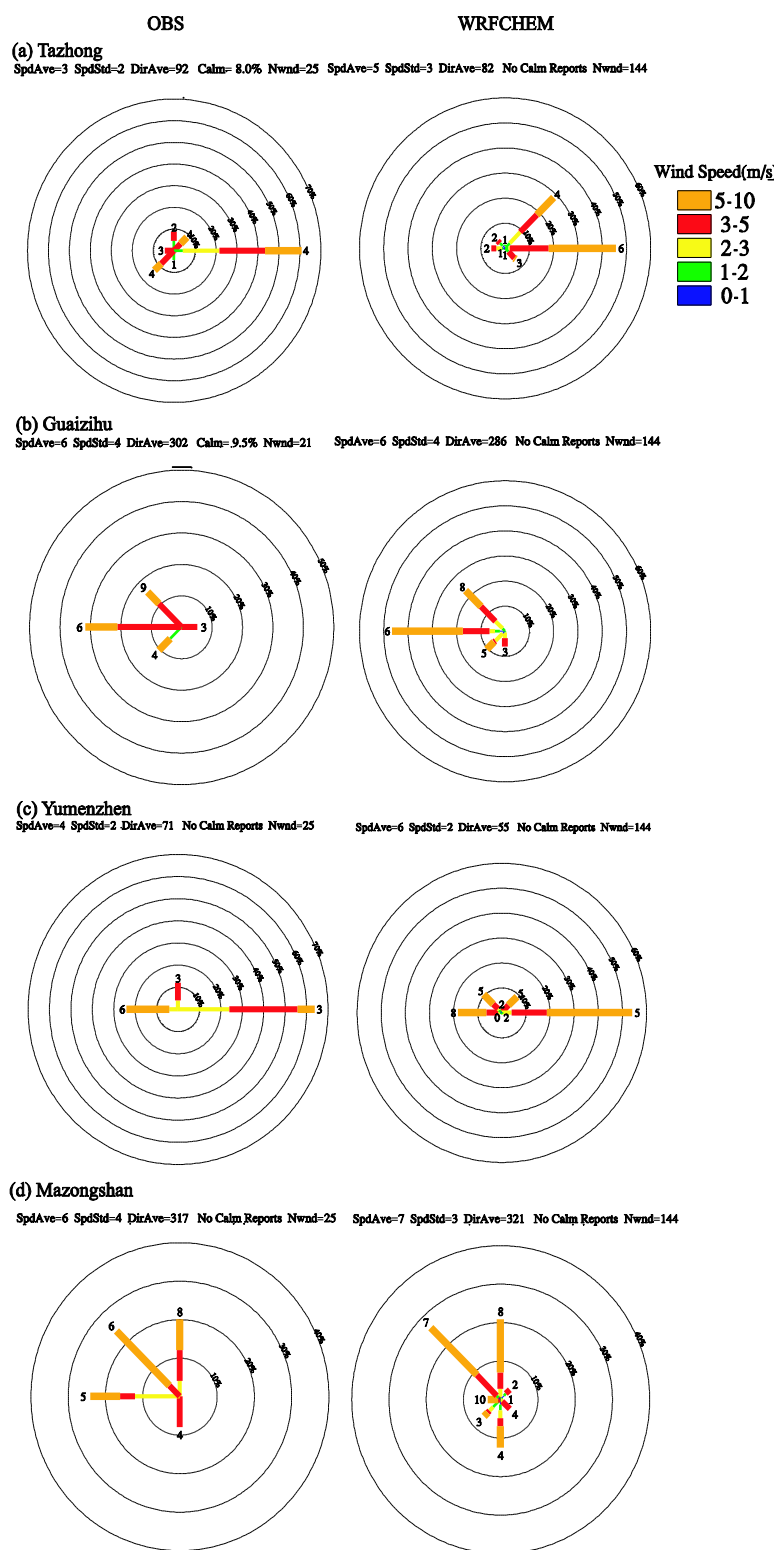
Fig. 3 Wind rose diagrams at the four meteorological stations: Tazhong (a), Guaizihu (b), Yumenzhen (c), and Maoyinbadao (d) over the TD and GD during the simulation period from observations and WRF-Chem model. The mean wind speed is included at the end of each directional line.

1123
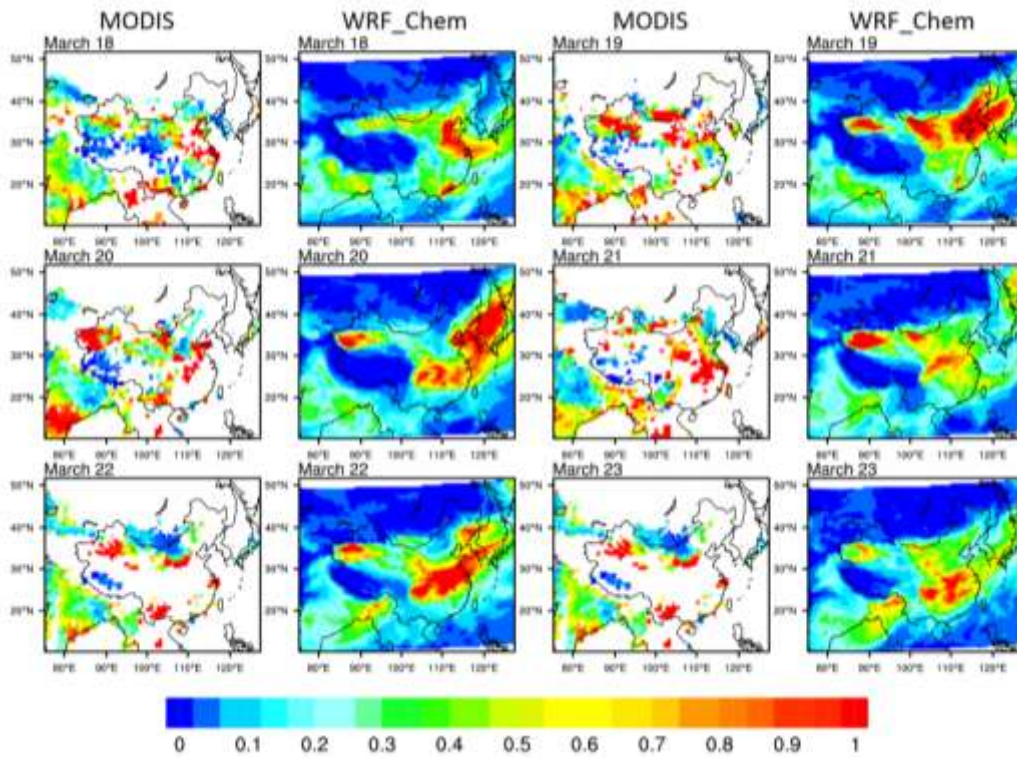
1124 Fig. 4 Spatial distributions of the daily mean 550-nm aerosol optical depths from the
1125 MODIS retrievals and the corresponding WRF-Chem simulations over East Asia
1126 during the simulation period.

1127

1128

1129

1130

1131
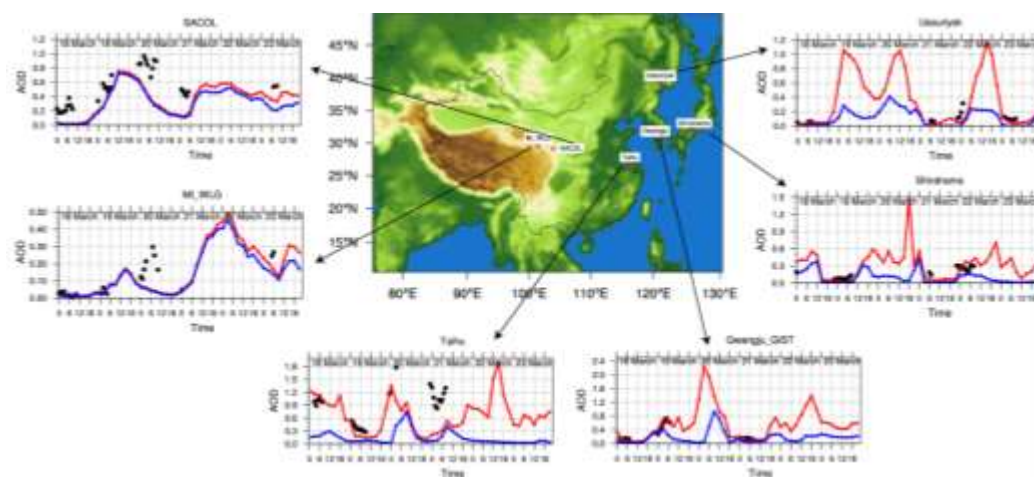
1132
1133 Fig. 5 Elevation map in the WRF-Chem domain and time series of the observed and
1134 modelled AOD at the six AERONET sites (SACOL, Taihu, Mt_Waliguan (Mt_WLG),
1135 Ussuriysk, Gwangju GIST, and Shirahama) during the simulation period. The black
1136 dots denote the 1 h averages of the observed AODs. The red and blue lines represent
1137 the modelled total and dust AODs from the WRF-Chem model, respectively.

1138
1139
1140
1141
1142
1143
1144
1145
1146
1147
1148
1149
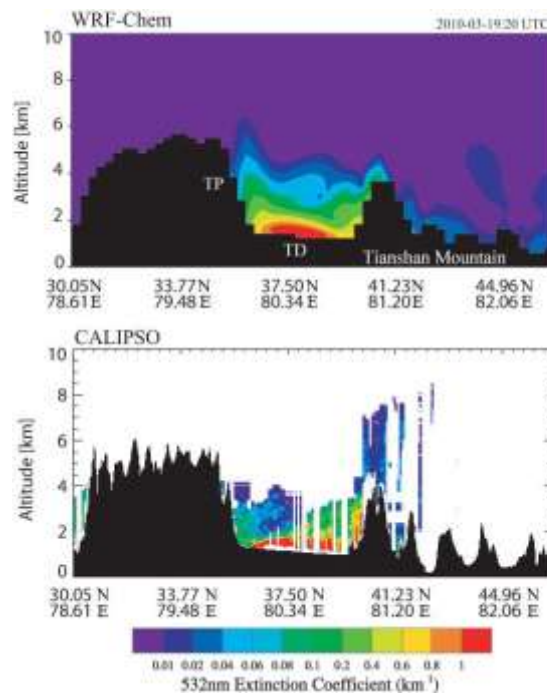
Fig. 6 Cross-sections of aerosol extinction coefficients at 532 nm (km^{-1}) over the TD at 20:08 UTC (2:08 LT) on 19th March 2010 from the WRF-Chem model (top) and CALIPSO retrievals (bottom) along the orbit path of CALIPSO (as shown in Fig. 1a).
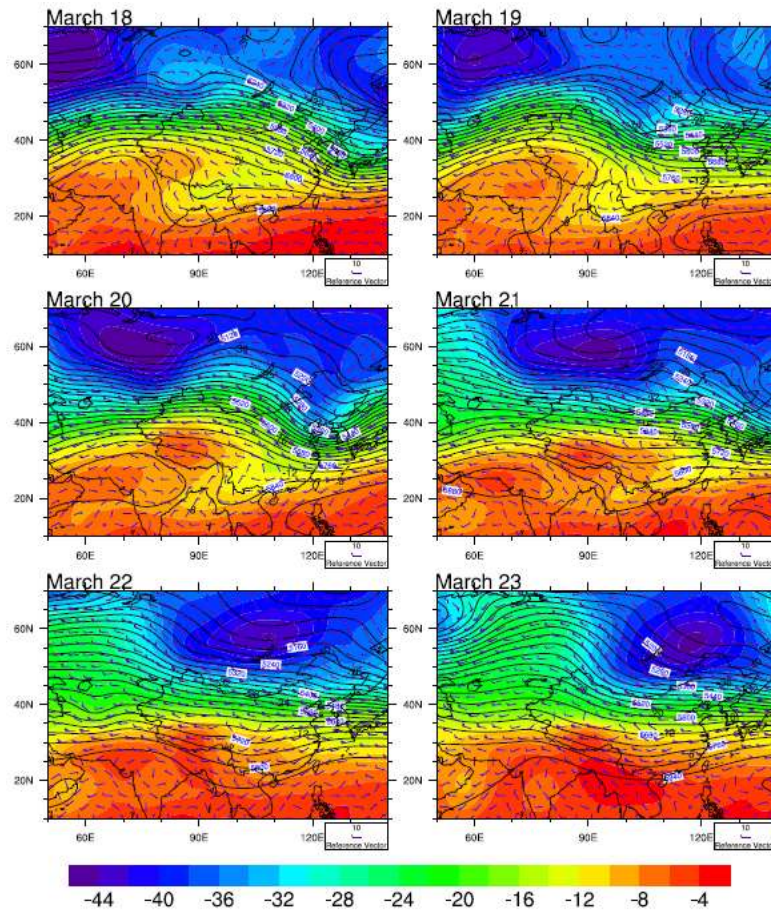
Fig. 7 Spatial distributions of geopotential heights (blue lines, unit: gpm), temperatures (color, unit: °C) at 500 hPa from the NCEP/FNL reanalysis data over East Asia during the simulation period. The vectors represent the wind field at 500 hPa (m s^{-1}).

March 18　　March 19

March 20　　March 21

March 22　　March 23

-24 -20 -16 -12 -8 -4 0 4 8 12 16 20 24
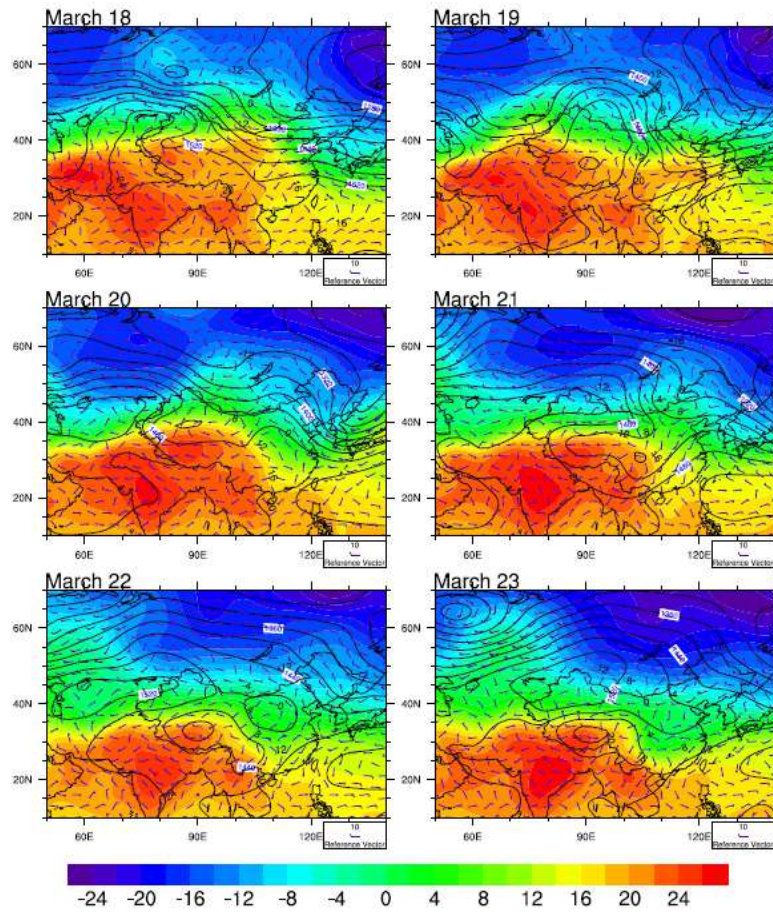
Fig.8 Spatial distributions of geopotential heights (blue lines, unit: gpm), temperatures (color, unit: °C) at 850 hPa from the NCEP/FNL reanalysis data over East Asia during the simulation period. The vectors represent the wind field at 850 hPa (m s^{-1}).

1170
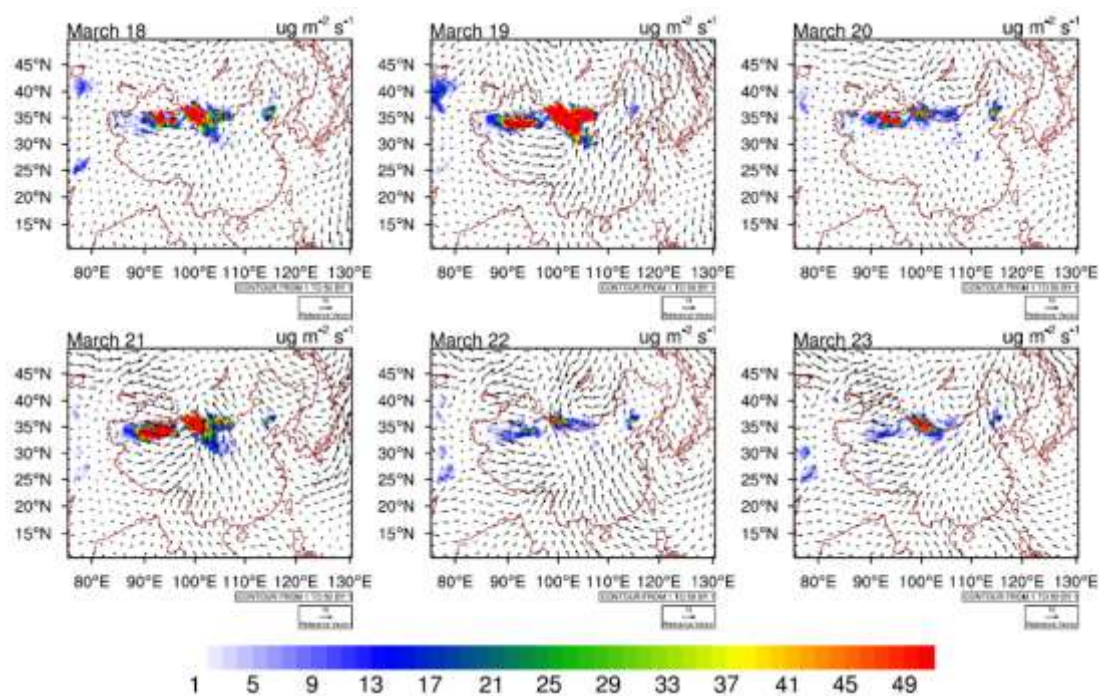
1171   Fig. 9 Spatial distributions of daily dust emission (μg m^{-2} s^{-1}) over East Asia during

1172   the simulation period from WRF-Chem simulations. The arrows represent the wind

1173   vectors at 10 m (m s^{-1}).

1174

1175
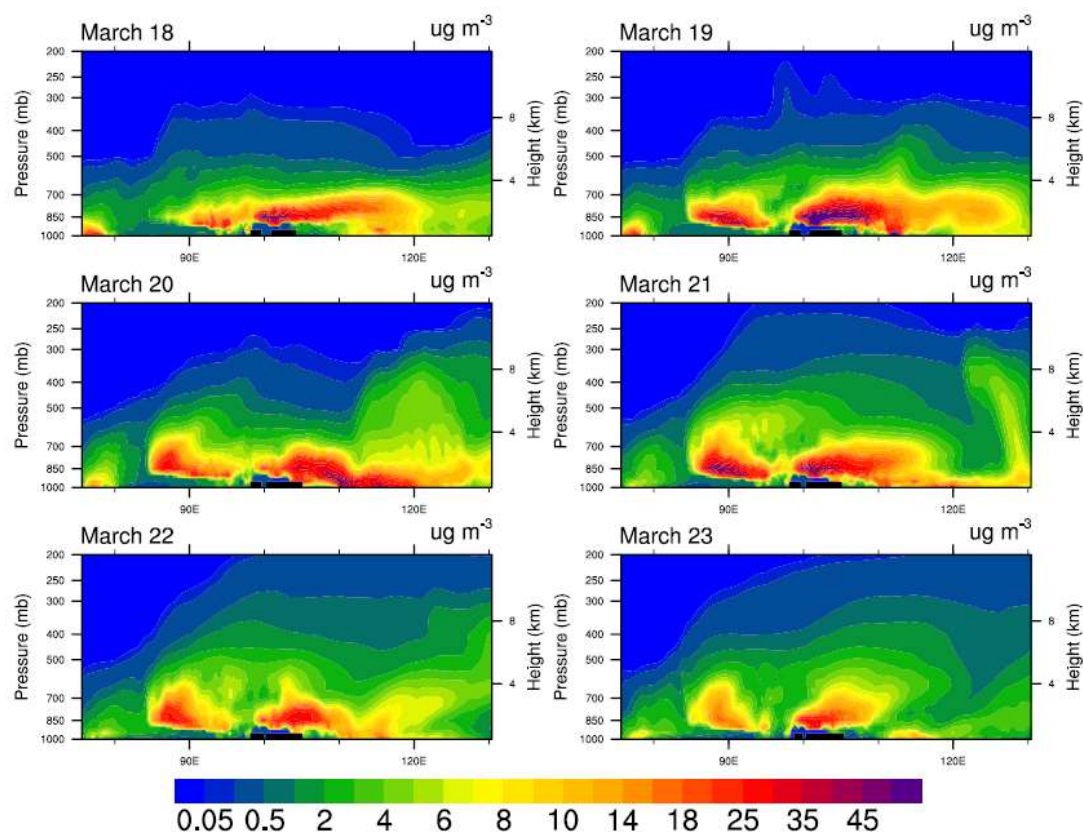
Fig. 10 Temporal and spatial cross sections of the meridional mean PM$_{2.5}$ dust concentration (ug m^{-3}) in the domain simulated by the WRF-Chem model during the simulation period.

1176
1177
1178

1179

1180

1181

1182

1183

1184

1185

1186
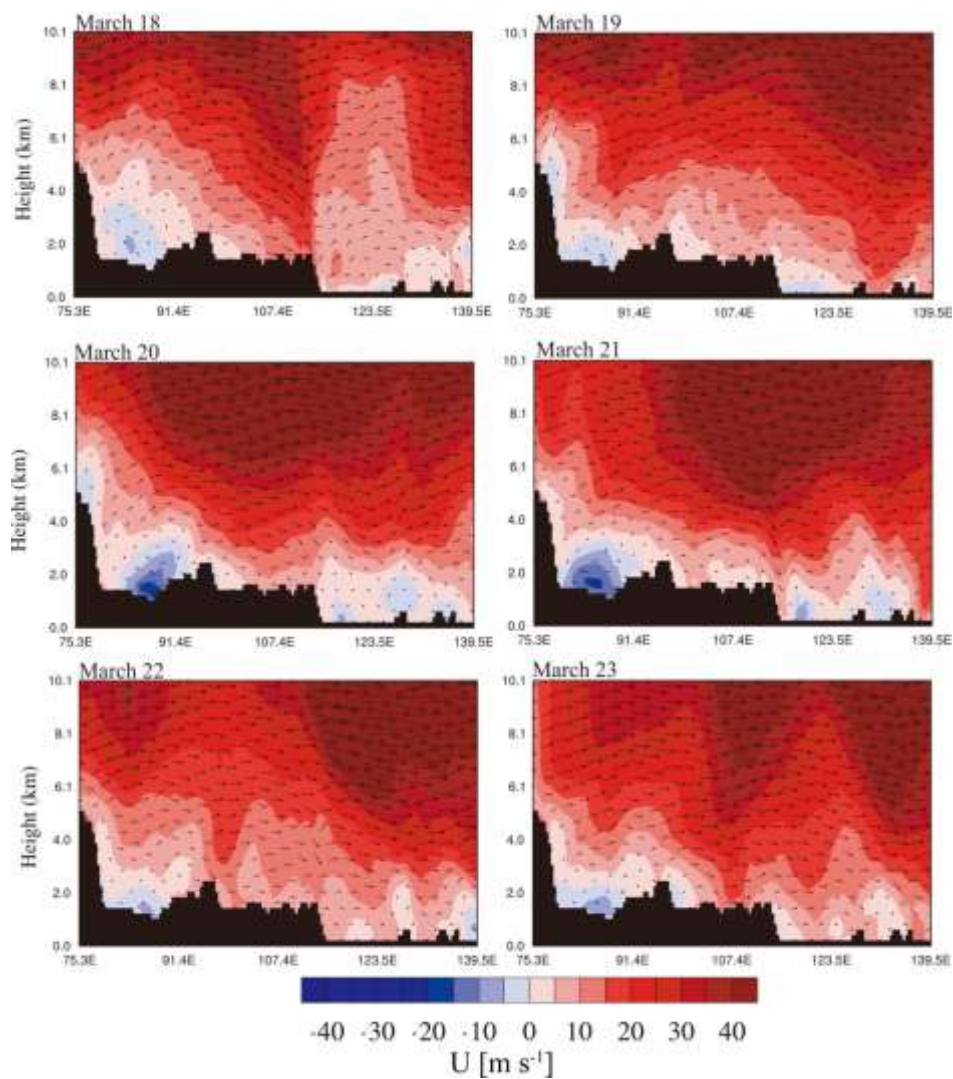
Fig. 11 Vertical-latitude cross section of zonal wind (m s^{-1}) and wind vector (the vertical wind scaled by 10^2) along 42°N during the simulation period from WRF-Chem simulation.
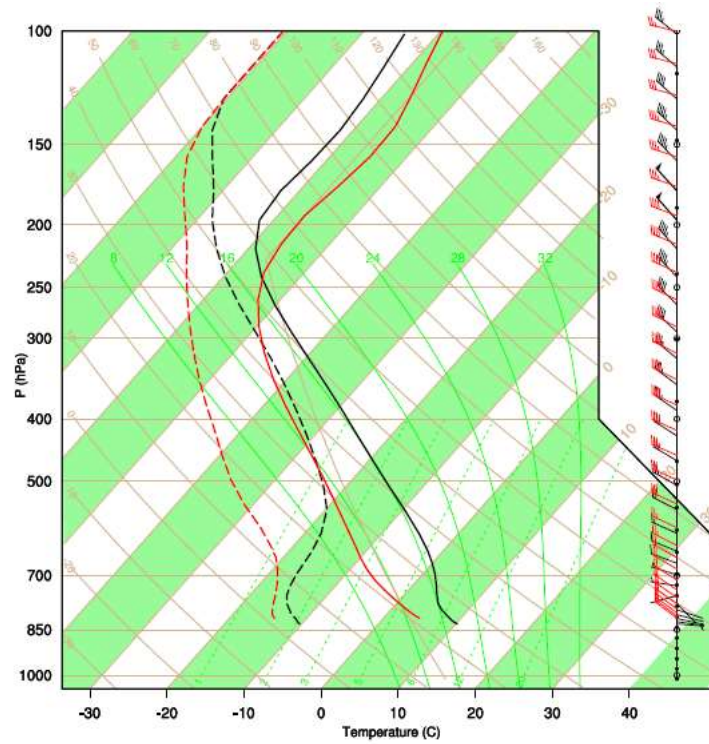
1190

1191
1192
1193
1194
1195
1196
1197

Fig.12 The skew T-log diagram over the TD (black lines) and GD (Red lines) on 19th March 2010 from the WRF-Chem simulation. The solid lines represent temperature and dash lines represent dew point temperature.
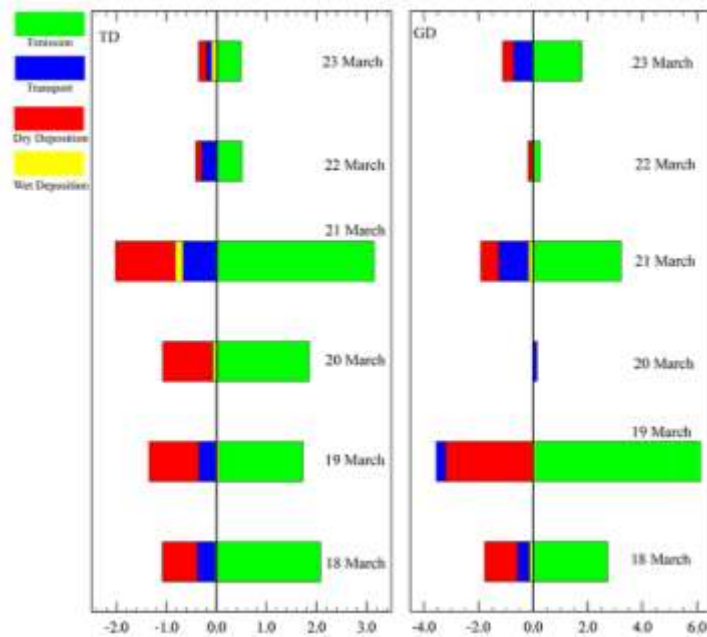
1210

Fig. 13 Average contributions of the dust emissions, transport, and dry and wet depositions to the dust mass balances over the TD and GD during the simulation period based on the WRF-Chem model. The positive sign represents increase to dust concentration and the negative sign represents decrease to dust concentration. Units: tons day^{-1}.
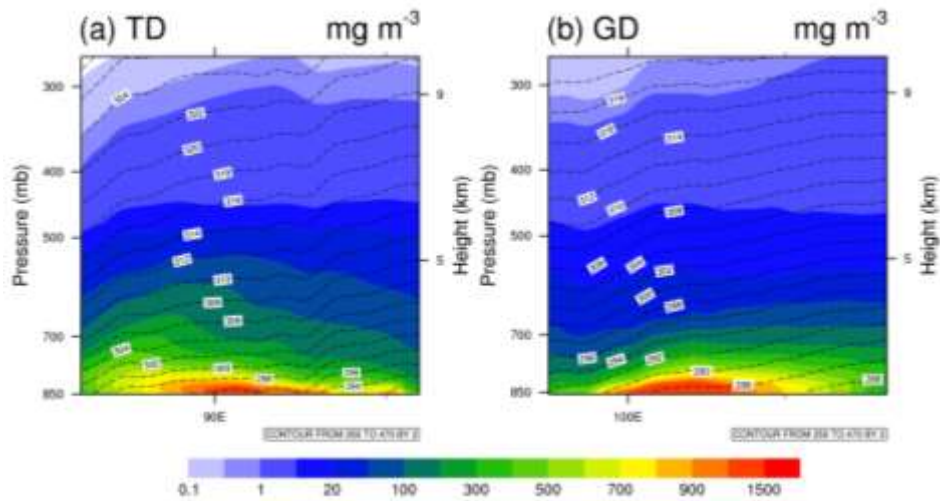
1216

1217

1218

1219

1220

1221

1222

1223

1224

1225

Fig. 14 Cross sections of the average dust mass concentrations (mg m⁻³) over the TD (Fig. 14a) and GD (Fig. 14b) during the simulation period based on the WRF-Chem model. The black lines represent potential temperature (K).
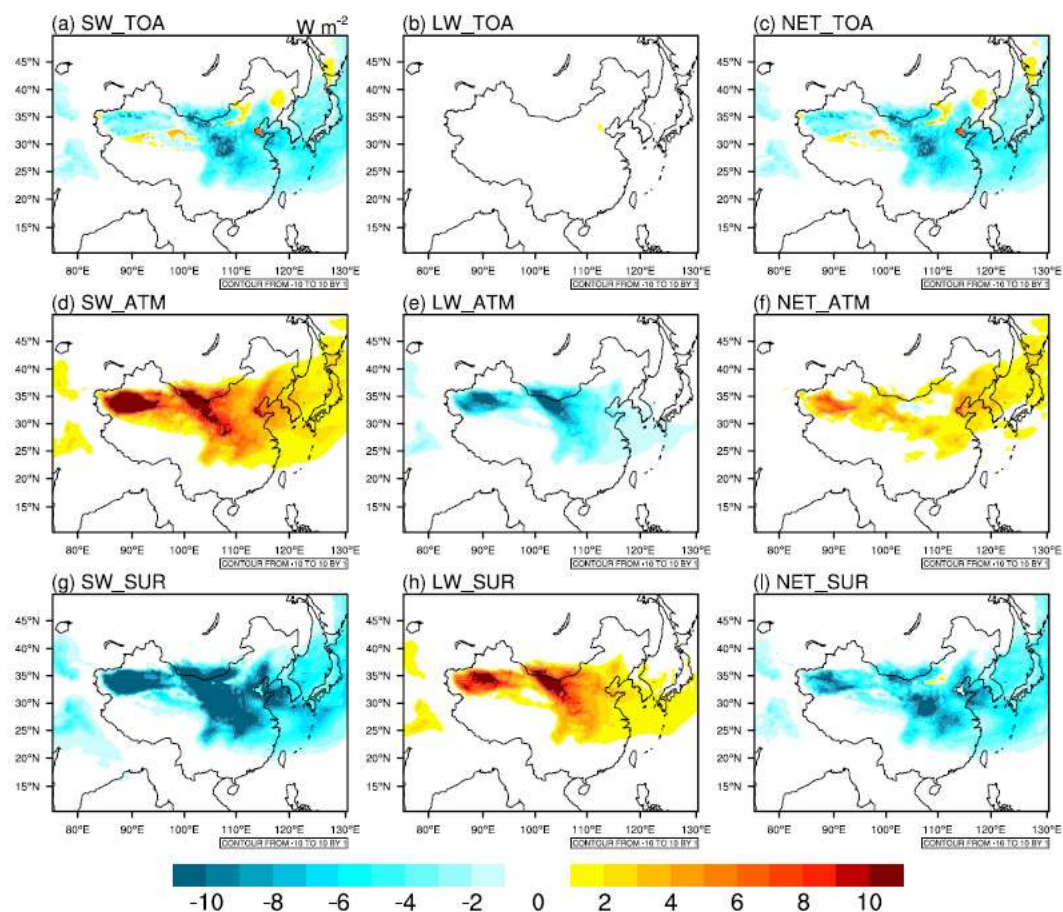
Fig. 15 Spatial distributions of dust direct radiative forcing for SW, LW, and net (SW+LW) radiation (W m^{-2}) at the TOA (top panels), SUR (bottom panels), and in the ATM (middle panels) average during the simulation period at all-sky conditions based on the WRF-Chem model. For dust direct radiative forcing, positive values at the TOA and SUR represent downward radiative fluxes, and represent radiative warming in the ATM.
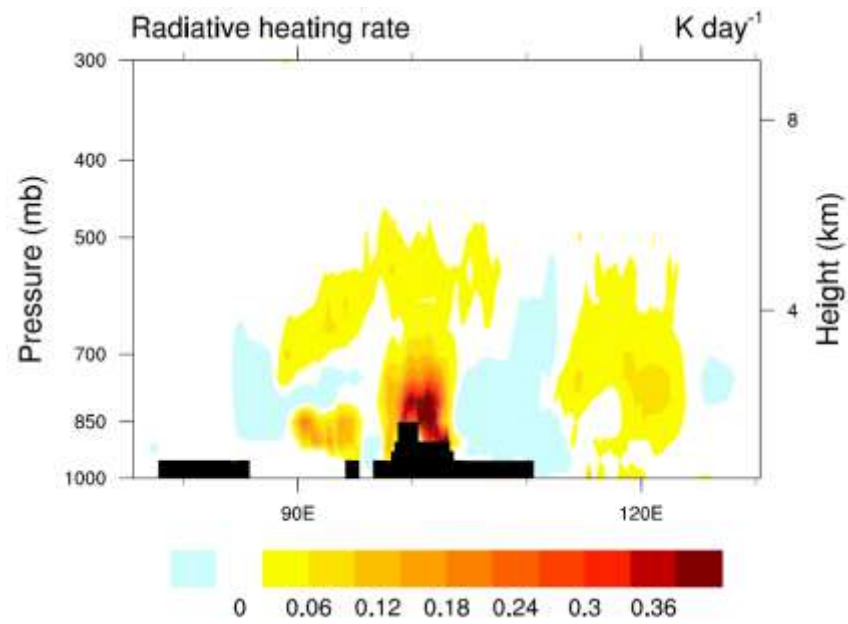
1245

1246 Fig. 16 Cross section of dust-induced radiative heating rate (K day^{-1}) from 15 N to

1247 45 N during the simulation period from WRF-Chem simulation.

1248

1249

1250

1251

1252

1253

1254